TABLE 1. Clinical Characteristics and *OPA1* Mutations in Patients with ADOA

Patient/ Age/Sex	Family	Visual Acuity (OD/OS)	Test Eye	Disk Appearance	Humphrey Visual Field MD (dB)	RNFL Thickness (μm)	*OPA1* Mutation	PhNR (μV)	OPs (μV)
1/24/M	92	0.04/0.05	OD	DA	−20.60	29.9*	p.S545R	17.3*	144.9
2/53/F	667	0.06/0.1	OD	TP	−8.30	71.6	p.R38X	19.3*	13.8*
3/27/F	42	0.4/0/4	OD	SP	−3.15	58.7*	c.2708_2711delTTAG	20.0*	96.6
4/46/M	169	0.3/0.3	OD	DA	−5.15	64.3*	c.2538insT	20.7*	62.1*
5/50/M	169	0.3/0.3	OS	DA	−10.34	52.9*	c.2538insT	22.4	55.2*
6/51/F	247	0.01/0.01	OD	DA	Not Recorded	44.7*	p.Q61X	20.7*	41.4*
7/55/M	247	0.7/0.7	OD	TP	−2.04	66.9*	p.Q61X	25.2	62.1*
8/22/M	526	0.15/0.15	OD	TP	−3.90	68.9	c.2591insC	22.4	75.9

RNFL thickness for control subjects was 102.0 ± 16.2 μm (range, 67.8–123.0 μm). DA, diffuse atrophy; TP, temporal pallor; SP, subtle temporal pallor; MD, mean deviation.

* Lower than normal range (see also Figs. 3, 4).

6), and normal fields in four patients (patients 4, 5, 7, 8). Humphrey static perimetry showed reduced sensitivity of different degrees; mean deviation within 30° borders of the visual field ranged from −2.04 to −20.60 dB. Reliable results of static perimetry could not be obtained from one patient (patient 6) because of unstable fixation. Color vision tests using panel D-15 plates showed normal results for two patients (patients 3, 7), a minor error for one patient (patient 8), blue-yellow defects in four patients (patients 1, 2, 4, 5), and failure with no specific axis (patient 6).

The average RNFL thickness around the optic disk was 57.2 ± 16.2 μm, which was approximately 56% that of control subjects of 102.0 ± 16.2 μm (Table 1). More details about the OCT findings in ADOA patients will be presented elsewhere.

Full-Field ERGs

Rod-cone mixed maximal ERGs and single-flash cone ERGs recorded from one representative control subject and eight ADOA patients are shown in Figures 1 and 2, respectively. Mean ± SD of each ERG component for the eight ADOA patients and 25 age-matched control subjects are shown in Table 2. Differences in the amplitudes of the rod ERG b-wave, the a- and b-waves of the mixed maximal ERG, and the a- and b-wave of single-flash cone ERG were not significant in the two groups, though the average amplitudes of the a- and b-waves of the mixed maximal ERG and the a- and b-wave of single-flash cone ERG were smaller in ADOA patients than in controls.

OPs were normal in one patient (patient 1) but were clearly reduced for the other seven patients and were nearly undetectable for five patients (patients 2, 5–8; Fig. 1). The mean amplitude of OPs for ADOA patients was 69.0 ± 39.0 μV, which was approximately half that for the control subjects (155.1 ± 65.4 μV). In five of eight patients (patients 2, 4–7; Fig. 3), the amplitude of the OPs was smaller than the lower limit for control subjects.

Because the amplitudes of the a- and b-waves were slightly smaller for ADOA patients than for control subjects, we were uncertain whether the reduction in OPs resulted from an overall reduction in ERG amplitude. To examine the relationship between the OPs and the a- and b-waves, we calculated a ratio of the amplitudes of OPs to the b-wave. The mean OPs/b-wave ratio was significantly lower in ADOA patients, indicating that the reduction in the amplitude of the OPs cannot be explained by a reduction in the overall ERG ($P = 0.001$; Table 2).

The reduction in the amplitude of the OPs was also dependent on the age of the patients. The reduction in the amplitudes of the OPs as a function of age for 25 age-matched controls and eight ADOA patients are shown in Figure 3. In the control subjects, no significant correlation was observed between OP amplitude and age ($r = 0.08$; $P = 0.75$). In contrast, a significant inverse correlation was observed between OP amplitude and age ($r = -0.78$; $P = 0.02$) for the ADOA patients. It was also noted that for patients older than 40, OP amplitude was smaller than the lowest amplitude of the control subjects (Fig. 3).

The PhNR was also significantly smaller for ADOA patients (21.0 ± 2.4 μV) than for control subjects (34.3 ± 9.0 μV; $P < 0.001$; Fig. 2; Table 2). The amplitude of the PhNR in five of the eight ADOA patients was lower than the lower limit of normal in control subjects (patients 1–4, 6; Fig. 4). We also calculated the ratio of the amplitudes of PhNR to the b-wave, and this ratio was also significantly reduced for the ADOA group ($P = 0.01$; Table 2).

TABLE 2. Amplitude of Each ERG Component for Control Subjects and ADOA Patients with *OPA1* Mutations

		Mixed Rod-Cone Maximal ERG			Cone ERG		
	Rod ERG b-Wave	a-Wave	b-Wave	OP (OP/b-Wave)	a-Wave	b-Wave	PhNR (PhNR/b-Wave)
Control	132.2 ± 37.8	322.6 ± 66.4	441.0 ± 104.5	155.1 ± 65.4 (0.36 ± 0.16)	33.4 ± 8.9	94.3 ± 28.9	34.3 ± 9.0 (0.40 ± 0.18)
Patient	133.3 ± 47.4	295.0 ± 55.5	432.1 ± 88.4	69.0 ± 39.0 (0.17 ± 0.10)	28.0 ± 5.6	85.0 ± 17.1	21.0 ± 2.4 (0.26 ± 0.07)
P	0.785	0.312	0.950	0.001 (0.001)	0.074	0.400	<0.001 (0.01)

Data are expressed as mean ± SD. Mann-Whitney *U* test was used for statistical comparison. $n = 25$ control subjects; $n = 8$ patients.

No significant correlation was observed between PhNR amplitude and age for control subjects ($r = -0.32$; $P = 0.09$) and for ADOA patients ($r = -0.41$; $P = 0.32$).

Correlation between ERG Amplitudes and RNFL Thickness or Psychophysical Measurements

Mean RNFL thickness around the optic disk, visual acuity, and mean deviation of static perimetry were not significantly correlated with PhNR and OP amplitudes.

Discussion

It has generally been thought that full-field ERGs are normal in patients with ADOA[26,27] because the primary abnormality of ADOA is the degeneration of ganglion cells.[7,8] Thus, Gränse et al.[26] examined the different components of the full-field ERGs in ADOA patients with *OPA1* mutations and reported that they were within the normal range for rod and cone components. Unfortunately, they did not analyze the ERG components that originate from inner retinal layers. In 1999, Holder et al.[28] reported that the N95 component of the pattern ERG, which is thought to originate from retinal ganglion cells, was lower than the normal limit in many ADOA patients and supported the idea that the fundamental abnormality of ADOA lies in the retinal ganglion cells.

In our analysis of eight ADOA patients with *OPA1* mutations, we found that PhNR amplitudes were significantly reduced. PhNR is a negative component of the photopic ERG seen after the b-wave, and it is thought to originate mainly from the activity of ganglion cells and their axons.[29,30] PhNR amplitude is reduced after blockage of the action potentials of ganglion cells by intravitreous injection of tetrodotoxin (TTX). It is also reduced in the eyes of monkeys with experimentally induced glaucoma.[29] In clinical studies, a selective reduction of the PhNR has been reported in patients with glaucoma[30,31] and optic nerve diseases.[32] Thus, it is not surprising to find that the mean PhNR amplitude in ADOA patients was approximately two thirds that of control subjects and that the amplitudes of the PhNR in five of eight patients were lower than the lower limit of normal in control subjects. These results support the idea that PhNR can be a useful objective indicator of the function of ganglion cells and their axons.

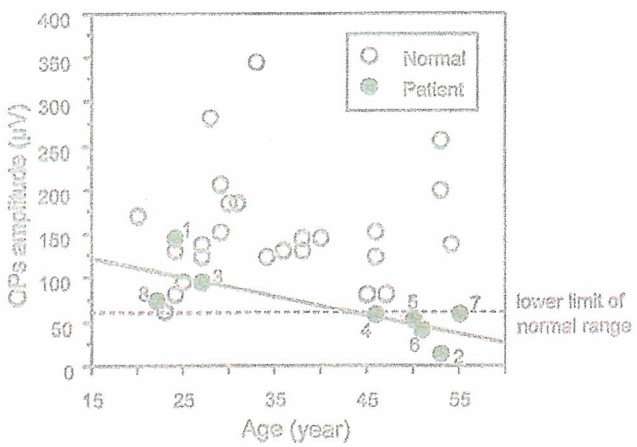

Figure 3. OP amplitude plotted as a function of age in 25 control subjects (○) and eight ADOA patients (●) with *OPA1* mutations. *Dotted line*: lower limit of normal range. *Solid line*: regression line between amplitude and age in the eight patients ($r = 0.78$; $P = 0.02$). The *number* shown near the ADOA patient (●) corresponds to the patient number in Table 1.

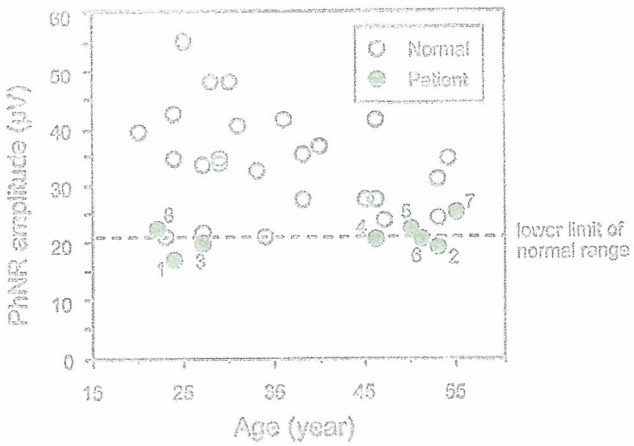

Figure 4. PhNR amplitude plotted as a function of age in 25 control subjects and eight ADOA patients with *OPA1* mutations. *Dotted line*: lower limit of normal range. The *number* shown near the ADOA patient (●) corresponds to the patient number in Table 1.

The most interesting finding in this study was the severe reduction in OP amplitude in ADOA patients. Thus, the mean OP amplitude in patients was less than half that in control subjects, and OP amplitude in four of eight patients was smaller than the lower limit of normal in control subjects. In addition, the strong inverse correlation between OP amplitude and age suggested progressive dysfunction of retinal neurons/circuits that gave rise to the OPs.

The origin of OPs has not been definitively determined, but OPs are generally thought to originate from feedback neural pathways in the inner retina, especially around the inner plexiform layer.[33,34] The cellular origin of OPs is thought to be mainly amacrine cells, though ganglion cells and bipolar cells may contribute to some parts of the OPs.[33–35] Our results strongly suggested that the *OPA1* gene is required not only for ganglion cell functioning but also for inner nuclear and plexiform layer—including amacrine cell—functioning. However, it is uncertain whether *OPA1* is directly related to the function of amacrine cells, where the *OPA1* gene is expressed, or whether the dysfunction of amacrine cells is secondary to ganglion cell degeneration.

Our results also indicated that the generators of the PhNR are affected severely in younger patients but that OP generators decrease slowly and progressively with age. Although the mechanism causing the gradual amplitude reduction of OPs is still undetermined, these different effects of the disease on the OPs and PhNRs may help to determine disease stage or severity.

A limitation of this study was that our patients were only relatively older patients—the youngest patient was 22—and therefore we could not analyze retinal function at earlier stages. Another limitation was that we did not record the ERGs from the same patient at different ages and thus could not state definitively the progressive nature of ADOA. Finally, our data did not differentiate whether the amplitude reduction of PhNR and OPs was specific to patients with *OPA1* mutations or more generally to optic atrophy. Further studies are needed to clarify the functional characteristics of the human retina arising from *OPA1* mutations.

References

1. Kjer P. Infantile optic atrophy with dominant mode of inheritance: a clinical and genetic study of 19 Danish families. *Acta Ophthalmol Scand.* 1959;37(suppl 54):1–146.

2. Kline LB, Glaser JS. Dominant optic atrophy: the clinical profile. *Arch Ophthalmol*. 1979;97:1680–1686.
3. Hoyt CS. Autosomal dominant optic atrophy: a spectrum of disability. *Ophthalmology*. 1980;87:245–251.
4. Votruba M, Fitzke FW, Holder GE, et al. Clinical features in affected individuals from 21 pedigrees with dominant optic atrophy. *Arch Ophthalmol*. 1998;116:351–358.
5. Johnston RL, Seller MJ, Behnam JT, et al. Dominant optic atrophy: refining the clinical diagnostic criteria in light of genetic linkage studies. *Ophthalmology*. 1999;106:123–128.
6. Miyake Y, Yagasaki K, Ichikawa H. Differential diagnosis of congenital tritanopia and dominantly inherited juvenile optic atrophy. *Arch Ophthalmol*. 1985;103:1496–1501.
7. Johnston PB, Gaster RN, Smith VC, Tripathi RC. A clinicopathologic study of autosomal dominant optic atrophy. *Am J Ophthalmol*. 1979;88:868–875.
8. Kjer P. Histopathology of eye, optic nerve and brain in a case of dominant optic atrophy. *Acta Ophthalmol*. 1982;61:300–312.
9. Delettre C, Lenaers G, Griffoin JM, et al. Nuclear gene OPA1, encoding a mitochondrial dynamin-related protein, is mutated in dominant optic atrophy. *Nat Genet*. 2000;26:207–210.
10. Alexander C, Votruba M, Pesch UE, et al. OPA1, encoding a dynamin-related GTPase, is mutated in autosomal dominant optic atrophy linked to chromosome 3q28. *Nat Genet*. 2000;26:211–215.
11. Pesch UE, Leo-Kottler B, Mayer S, et al. OPA1 mutations in patients with autosomal dominant optic atrophy and evidence for semi-dominant inheritance. *Hum Mol Genet*. 2001;10:1359–1368.
12. Toomes C, Marchbank NJ, Mackey DA, et al. Spectrum, frequency and penetrance of OPA1 mutations in dominant optic atrophy. *Hum Mol Genet*. 2001;10:1369–1378.
13. Thiselton DL, Alexander C, Morris A, et al. A frameshift mutation in exon 28 of the OPA1 gene explains the high prevalence of dominant optic atrophy in the Danish population: evidence for a founder effect. *Hum Genet*. 2001;109:498–502.
14. Delettre C, Lenaers G, Pelloquin L, et al. OPA1 (Kjer type) dominant optic atrophy: a novel mitochondrial disease. *Mol Genet Metab*. 2002;75:97–107.
15. Thiselton DL, Alexander C, Taanman JW, et al. A comprehensive survey of mutations in the *OPA1* gene in patients with autosomal dominant optic atrophy. *Invest Ophthalmol Vis Sci*. 2002;43:1715–1724.
16. Nakamura M, Lin J, Ueno S, et al. Novel mutations in *OPA1* gene and associated clinical features in Japanese patients with optic atrophy. *Ophthalmology*. 2006;113:483–488.
17. Nakamura M, Miyake Y. Optic atrophy and negative electroretinogram in a patient associated with a novel OPA1 mutation. *Graefes Arch Clin Exp Ophthalmol*. 2006;244:274–275.
18. Olichon A, Emorine LJ, Descoins E, et al. The human dynamin-related protein OPA1 is anchored to the mitochondrial inner membrane facing the inter-membrane space. *FEBS Lett*. 2002;523:171–176.
19. Olichon A, Baricault L, Gas N, et al. Loss of OPA1 perturbates the mitochondrial inner membrane structure and integrity, leading to cytochrome *c* release and apoptosis. *J Biol Chem*. 2003;278:7743–7746.
20. Kamei S, Chen-Kuo-Chang M, Cazevieille C, et al. Expression of the Opa1 mitochondrial protein in retinal ganglion cells: its downregulation causes aggregation of the mitochondrial network. *Invest Ophthalmol Vis Sci*. 2005;46:4288–4294.
21. Yoon Y, McNiven MA. Mitochondrial division: new partners in membrane pinching. *Curr Biol*. 2001;11:R67–70.
22. Misaka T, Miyashita T, Kubo Y. Primary structure of a dynamin-related mouse mitochondrial GTPase and its distribution in brain, subcellular localization, and effect on mitochondrial morphology. *J Biol Chem*. 2002;277:15834–15842.
23. Aijaz S, Erskine L, Jeffery G, et al. Developmental expression profile of the optic atrophy gene product: OPA1 is not localized exclusively in the mammalian retinal ganglion cell layer. *Invest Ophthalmol Vis Sci*. 2004;45:1667–1673.
24. Pesch UE, Fries JE, Bette S, et al. *OPA1*, the disease gene for autosomal dominant optic atrophy, is specifically expressed in ganglion cells and intrinsic neurons of the retina. *Invest Ophthalmol Vis Sci*. 2004;45:4217–4225.
25. Ju WK, Misaka T, Kushnareva Y, et al. OPA1 expression in the normal rat retina and optic nerve. *J Comp Neurol*. 2005;488:1–10.
26. Gränse L, Bergstrand I, Thiselton D, et al. Electrophysiology and ocular blood flow in a family with dominant optic nerve atrophy and a mutation in the *OPA1* gene. *Ophthalmic Genet*. 2003;24:233–245.
27. Yagasaki K, Miyake Y, Awaya S, et al. ERG (electroretinogram) in hereditary optic atrophies (in Japanese). Nippon Ganka Gakkai Zasshi 1986;90:124–130.
28. Holder GE, Votruba M, Carter AC, et al. Electrophysiological findings in dominant optic atrophy (DOA) linking to the OPA1 locus on chromosome 3q 28-qter. *Doc Ophthalmol*. 1998–99;95:217–228.
29. Viswanathan S, Frishman LJ, Robson JG, et al. The photopic negative response of the macaque electroretinogram: reduction by experimental glaucoma. *Invest Ophthalmol Vis Sci*. 1999;40:1124–1136.
30. Viswanathan S, Frishman LJ, Robson JG, Walters JW. The photopic negative response of the flash electroretinogram in primary open angle glaucoma. *Invest Ophthalmol Vis Sci*. 2001;42:514–522.
31. Colotto A, Falsini B, Salgarello T, et al. Photopic negative response of the human ERG: losses associated with glaucomatous damage. *Invest Ophthalmol Vis Sci*. 2000;41:2205–2211.
32. Gotoh Y, Machida S, Tazawa Y. Selective loss of the photopic negative response in patients with optic nerve atrophy. *Arch Ophthalmol*. 2004;122:341–346.
33. Heynen H, Wachtmeister L, van Norren D. Origin of the oscillatory potentials in the primate retina. *Vision Res*. 1985;25:1365–1373.
34. Wachtmeister L. Oscillatory potentials in the retina: what do they reveal. *Prog Retin Eye Res*. 1998;17:485–521.
35. Rangaswamy NV, Zhou W, Harwerth RS, Frishman LJ. Effect of experimental glaucoma in primates on oscillatory potentials of the slow-sequence mfERG. *Invest Ophthalmol Vis Sci*. 2006;47:753–767.

Japanese Journal of Applied Physics
Vol. 45, No. 19, 2006, pp. L505–L507

Optimization of Electrical Stimulus Pulse Parameter for Low-Power Operation of Retinal Prosthetic Device

Tetsuo FURUMIYA, Shinya YAMAMOTO, Keiichiro KAGAWA, Takashi TOKUDA, Masahiro NUNOSHITA and Jun OHTA*

Graduate School of Material Science, Nara Institute of Science and Technology, 8916-5 Takayama, Ikoma, Nara 630-0101, Japan

(Received January 1, 2006; accepted March 27, 2006; published online May 12, 2006)

In this paper, we describe the investigation of an electrical stimulus pulse parameter for use in a low-power retinal prosthesis. To obtain efficient stimulus pulse parameters, *in vitro* electrical stimulus experiments with a detached frog retina were performed using a fabricated pulse-frequency modulation (PFM) image sensor as a retinal prosthesis. The evaluated electrical stimulus pulse parameters were pulse duration, pulse amplitude, and the number of pulses. From the experiments, the firing rate of the retinal ganglion cells (retinal ganglion cells; RGCs) was observed to depend on the injection charge in single-pulse stimulation and the injection charge of the first pulse in pulse-train stimulation. In addition, pulse-train stimulation was found to have a RGC firing rate lower than that of single-pulse stimulation at the same injection charge. From power consumption measurements and an *in vitro* experiment, it was verified that the stimulus pulse of a short-pulse duration is suitable for use in a low-power retinal prosthesis. [DOI: 10.1143/JJAP.45.L505]

KEYWORDS: retinal prosthesis, CMOS image sensor, pulse-frequency modulation, stimulus pulse parameter, *in vitro* electrophysiological experiment, power consumption

The goal of this research is to develop an implantable retinal prosthesis that provides an electrical stimulus to the retina, to reproduce visual sensation in blind patients with severe retinitis pigmentosa (RP) or age-related macular degeneration (AMD). RP and AMD cause various degrees of irreversible vision loss due to a substantial loss of photoreceptor cells in tens of millions of people worldwide. However, patients suffering from RP and AMD typically have intact retinal cells, which are unrelated to photoreceptor cells. The electrical excitation of these retinal cells by an implanted device has been reported to be an effective approach for producing a partial recovery of visual sensation in blind patients. One approach involves implanting a silicon-based retinal prosthesis that converts incident light into an electrical stimulus, thereby replacing the function of damaged photoreceptor cells.[1–4]

To develop an effective retinal prosthesis, it is necessary to output a sufficient injection charge to electrically stimulate retinal cells. To obtain a sufficient injection charge, an active device such as a retinal prosthesis with a pulse-frequency modulation (PFM) photosensor has been proposed.[5] The device is implanted between the retina and retinal pigment epithelium (subretinal space) and generates the electrical stimulus for the retinal cells. The PFM photosensor converts incident light into a digital pulse stream at a frequency that is proportional to the light intensity.[6] The PFM photosensor can be improved by implementing image processing, to stimulate retinal cells more effectively.[7,8] A fabricated PFM image sensor for retinal prosthesis was applied in *in vivo* electrophysiological experiments using a frog retina, and its ability to effectively stimulate retinal cells has been verified.[9]

However, to implant a retinal prosthesis in an eyeball, power must be supplied wirelessly (RF or light transmission, etc.). A low-power retinal prosthesis is required because the maximum transfer power for RF in the implant environment is only a few tens of mW.[10] The power consumption of the stimulus unit is larger than that of the photosensing unit. For this reason, an electrical stimulus signal has been investigated. If a signal that is suitable for a retinal cells stimulus is used, then power consumption can be decreased. However, the parameter (amplitude, duration, etc.) that is most suitable for the retinal cell stimulus has yet to be determined. In the case of the retinal prosthesis, it is necessary to set up a stimulus pulse parameter for each pixel because the stimulus electrode state, the distance from retinal cells, and the firing rate of retinal cells differ for each pixel. To determine an efficient stimulus pulse parameter, *in vitro* electrical stimulus experiments have been performed on a detached frog retina using the fabricated PFM image sensor as a retinal prosthesis.

Bullfrogs (*Rana catesbeiana*, 10–12 cm in length) were dark adapted for 20–30 min and then their retinas were surgically removed under dim illumination. One eyeball was enucleated and hemisected. The other eyeball was also enucleated, soaked in Ringer solution, and kept in a refrigerator for the next experiment. After the cornea and lens were removed, the sclera was separated from the pigment epithelium. The retina was then isolated from the pigment epithelium. A piece of retina approximately 3–5 mm wide was cut from the central part of the retina, and positioned [retinal ganglion cell (RGC) side up] on the surface of the packaged image sensor. Figure 1(a) shows the experimental setup. The retina was rinsed in a chamber with a Ringer solution and was fixed using a piece of ring-shaped filter paper after the Ringer solution was removed. The Ringer solution consisted of (in mM) NaCl (100), KCl (3.3), $CaCl_2$ (2), $MgCl_2$ (1), Glucose (10), and HEPES (10).

Experiments were carried out under microscope observation with infrared (IR)-sensitive optics (Olympus). Images were captured using an IR CCD camera (Texas Instruments). To confirm the condition of the retinal cells and the position of the recording electrode, light stimulation was given at the start of the experiment. After recording the light-induced RGC response, electrical stimulation was given in a stimulator mode using a single pixel selected from the image sensor. A tungsten stimulus reference electrode (World Precision Instruments; impedance, 0.1 MΩ) was placed on the retina to produce a transretinal current and the position of the tungsten electrode was controlled using a

*E-mail address: ohta@ms.naist.jp

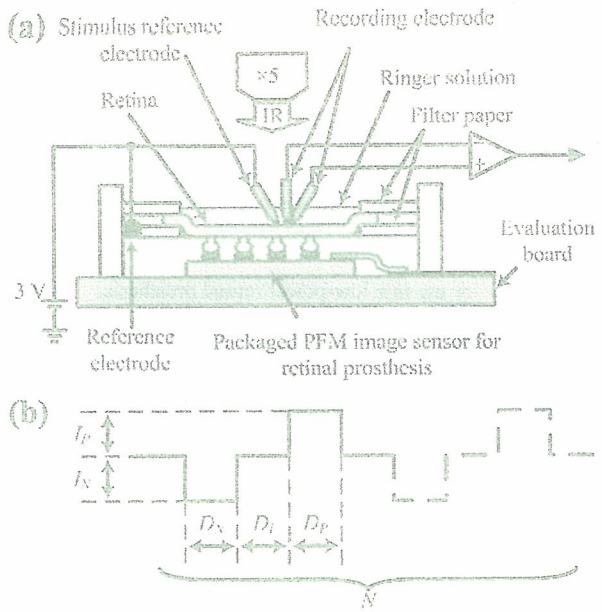

Fig. 1. (a) Experimental setup. (b) Stimulus pulse used in the experiment.

Table I. Details of stimulus pulse used in experiment.

			1	2	3	4	5
Q-Low	Amplitude (I)	μA	28	14	8	106	28
	Duration (D)	μs	500	1000	2000	100	100
	Number (N)	pulses	1	1	1	1	5
	Charge (C)	nC	14	14	16	10.6	14
Q-Mid	Amplitude (I)	μA	54	28	14	106	54
	Duration (D)	μs	500	1000	2000	100	100
	Number (N)	pulses	1	1	1	3	5
	Charge (C)	nC	27	28	28	31.8	27
Q-Hi	Amplitude (I)	μA	106	54	28	106	—
	Duration (D)	μs	500	1000	2000	100	—
	Number (N)	pulses	1	1	1	5	—
	Charge (C)	nC	53	54	56	53	—

manipulator (Micronics Japan). Figure 1(b) shows a schematic of the investigated stimulus pulse. The stimulus pulse parameters are current amplitude (I) (positive, I_P; negative, I_N), pulse duration (D) (positive, D_P; negative, D_N), interpulse duration (D_I), and pulse number (N). The stimulus pulse used in the experiment is a negative-first biphasic current pulse, and stimulus efficiency is compared using three injection charge group: approximately 14, 28, and 54 μA (14 pulses). Table I shows the details of the stimulus pulse used in the experiment. The inter-pulse durations were 1 ms for single-pulse stimulation ($D_P = D_N = 500$ to 2000 μs) and 100 μs for pulse-train stimulation ($D_P = D_N = 100$ μs). The spacing is 100 μs for pulse-train stimulation. Stimuli were applied 10 times for each pulse at intervals of 1.5 s. After electrical stimulation, light stimulation was performed again to confirm that the same response at that caused by the initial stimulation was obtained.

To reduce the effects of artifacts and noise, two carbon fiber electrodes (World Precision Instruments; tip diameter, 30 μm,) were used for the bipolar recording of the extracellular response of the RGCs. The positions of the

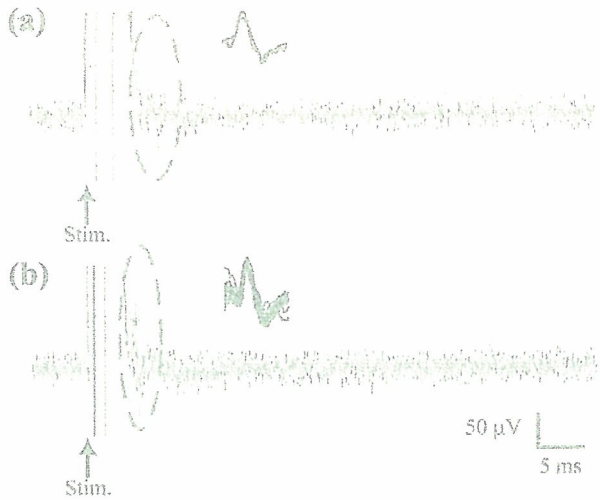

Fig. 2. Electrical stimulus-induced response of RGCs (superposition of 10 stimuli). (a) Q-Low 3, (b) Q-Hi 2.

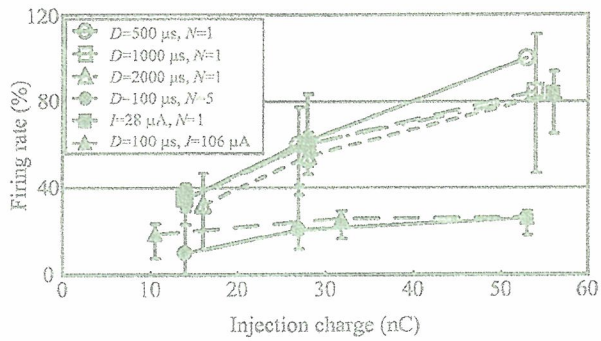

Fig. 3. Experimental results showing the relationship between firing rate of RGC spikes and injection charge ($n = 5$).

carbon electrodes were controlled using two manipulators (Narishige). The distance between the two carbon electrodes was set at about 100 μm, and the distance between the carbon electrode pair and the tungsten electrode was set at about 100 μm. An Ag/AgCl wire was used as the reference in the chamber. The recorded response was amplified using an AC differential amplifier (World Precision Instruments; 0.3–10 kHz, 10000×). The amplified signal was sampled by a computer via an analog-to-digital converter (ADC) (Cambridge Electronic Design; 20 kHz, 16 bit). The sampled data were analyzed using spike-detecting software (Cambridge Electronic Design) with the spike detection threshold set at three-fold higher than the floor level.

The induced activity was recorded at twenty two locations on seven retinas. Figure 2 shows the electrically induced RGC response. Figure 3 shows the dependence of firing rate on injection charge. Firing rate was standardized and the maximum spike number was obtained with Q-Hi 1 in Table I. This result indicates that firing rate increases with stimulus pulse amplitude in the single-pulse stimulation of each pulse duration and with stimulus pulse duration in the single-pulse stimulation. However, firing rate did not depend on the number of pulses. In the pulse-train stimulation, firing rate increases with stimulus pulse amplitude and was lower than that for single-pulse stimulation.

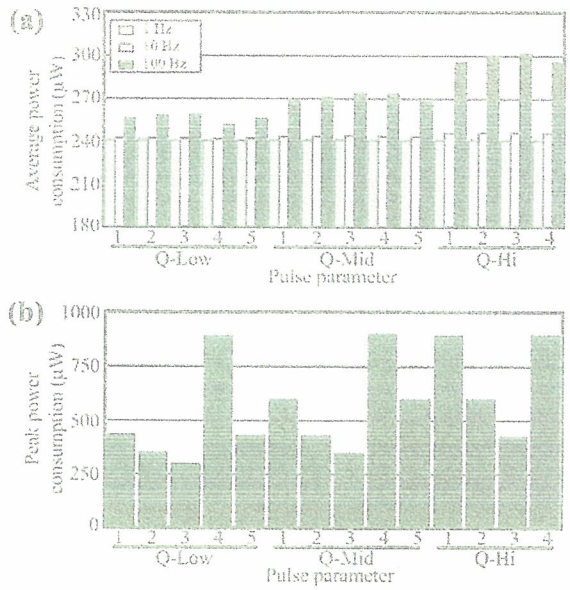

Fig. 4. Experimental results. (a) Average power consumption and (b) peak power consumption of stimulus current generator on each pulse parameter. The plot shows pulse parameters from Q-Low 1 on the left to Q-Hi 4 on the right.

Figure 4 shows the relationship between the power consumption of the stimulus current generation and stimulus pulse parameter. The power consumption of stimulus current generation at each stimulus pulse parameter was measured using an ampere meter (Keithley Instruments). The measured stimulus frequencies were 1, 10, and 100 Hz. The stimulus current was output to a 10 kΩ resistor instead of the stimulus electrode. This is because, in order to reach 100 μA or more of output current when the power supply voltage of the image sensor is 6 V, the maximum admissible load resistance is about 10 kΩ. The standby power requirement of this circuit was 240.15 μW. The maximum average power consumption was 301.50 μW in Q-Hi 3. The maximum peak power consumption was 876.15 μW in Q-Low 4, Q-Mid 4, Q-Hi 1, and Q-Hi 4. In the case of the same injection charge, when pulse duration doubled, average power consumption minus the standby power increased by 11% and the peak power consumption minus standby power decreased 45%. This result indicates that a short-pulse duration is suitable for reducing peak power consumption and a long-pulse duration is suitable for reducing average power consumption.

Based on the results of *in vitro* electrophysiological and power consumption experiments, single-pulse stimulation is suitable for use in retinal prostheses. These results also show that a short-pulse duration is suitable for reducing average power consumption, while a long-pulse duration is suitable for reducing peak power consumption. Moreover, the peak power consumption of a retinal prosthesis, not the average need, should be considered with regard to the maximum RF transmitted power. For example, when the maximum RF transmitted power is 50 mW, the maximum stimulus pixel numbers are 63 pixels in Q-Hi 1 and 118 pixels in Q-Hi 3. However these pixel numbers are insufficient to reproduce visual sensation. If the stimulus timing is shifted for each pixel (each column or row), then a device with a few hundred stimulus pixels could be realized. Considering average power consumption, a short-pulse duration would be more suitable for use in a retinal prosthesis.

In summary, the stimulus pulse parameter was investigated to realize a low-power retinal prosthesis. *In vitro* electrophysiological experiments with detached frog retinas using the fabricated PFM image sensor as a retinal prosthesis were performed and the stimulus efficiency of single-pulse and pulse-train stimulations were determined. The results revealed that single-pulse stimulation is suitable for use in retinal prostheses. Power consumption measurements verified that a short-pulse duration is suitable for reducing peak power consumption and a long-pulse duration is suitable for reducing average power consumption. Finally, the experiments indicated the possibility of reducing the peak and average power consumptions of a multisite stimulation. Future research is needed to reduce the standby power requirement. In addition, the further investigation of stimulus electrode material and the determination of the RGC response to multisite stimulation are needed.

Acknowledgements

The authors thank Professor Tetsuya Yagi of Osaka University for his comments on the *in vitro* electrophysiological experiments, and Professors Yasuo Tano and Takashi Fujikado of Osaka University for their continuous encouragement. We would also like to thank David C. Ng for his comments and help in checking the manuscript. This work was partially supported by the New Energy and Industrial Technology Development Organization (NEDO) of Japan, and Health and Labor Science Research Grants, Japan.

1) A. Y. Chow, M. T. Pardue, V. Y. Chow, G. A. Peyman, C. Liang, J. I. Perlman and N. S. Peachey: IEEE Trans. Neural Syst. Rehabil. Eng. **9** (2001) 86.
2) E. Zrenner: Science **295** (2002) 1022.
3) E. Margalit, M. Maia, J. D. Weiland, R. J. Greenberg, G. Y. Fujii, G. Tores, D. V. Piyathaisere, T. M. O'Hearn, W. Liu, G. Lazzi, G. Dagnelie, D. A. Scribner, E. de Juan, Jr. and M. S. Humayun: Surv. Ophthalmol. **47** (2002) 335.
4) J. Deguchi, T. Watanabe, T. Nakamura, Y. Nakagawa, T. Fukushima, Shim Jeoung-Chill, H. Kurino, T. Abe, M. Tamai and M. Koyanagi: Jpn. J. Appl. Phys. **43** (2004) 1685.
5) J. Ohta, N. Yoshida, K. Kagawa and M. Nunoshita: Jpn. J. Appl. Phys. **41** (2002) 2322.
6) F. Andoh, H. Shimamoto and Y. Fujita: IEEE Trans. Electron Devices **47** (2000) 2123.
7) K. Kagawa, K. Isakari, T. Furumiya, A. Uehara, T. Tokuda, J. Ohta and M. Nunoshita: Electron. Lett. **39** (2003) 419.
8) K. Kagawa, K. Yasuoka, D. C. Ng, T. Furumiya, T. Tokuda, J. Ohta and M. Nunoshita: IEEE J. Sel. Top. Quantum Electron. **10** (2004) 816.
9) T. Furumiya, D. C. Ng, K. Yasuoka, K. Kagawa, T. Tokuda, M. Nunoshita and J. Ohta: Biosens. Bioelectron. **21** (2006) 1059.
10) M. Sawan, Y. Hu and J. Coulombe: IEEE Circuit Syst. Mag. **5** (2005) 21.

Pulse Frequency Modulation Based CMOS Image Sensor for Subretinal Stimulation

David C. Ng, *Student Member, IEEE*, Tetsuo Furumiya, Koutaro Yasuoka, Akihiro Uehara, Keiichiro Kagawa, Takashi Tokuda, Masahiro Nunoshita, *Member, IEEE*, and Jun Ohta, *Member, IEEE*

Abstract—We have developed a CMOS image sensor based on pulse frequency modulation for subretinal implantation. The sensor chip forms part of the proposed intraocular retinal prosthesis system where data and power transmission are provided wirelessly from an extraocular unit. Image sensing and electrical stimulus are integrated onto the same chip. Image of sufficient resolution has been demonstrated using 16 × 16 pixels. Biphasic current stimulus pulses at above threshold levels of the human retina (500 μA) at varying frame rates (4 Hz to 6 kHz) have been achieved. The implant chip was fabricated using standard CMOS technology.

Index Terms—CMOS image sensor, pulse-frequency modulation (PFM), retinal prosthesis, subretinal implant.

I. Introduction

An ESTIMATED 50000 people in Japan and 1500000 people worldwide are blind because of photoreceptor deterioration due to retinitis pigmentosa (RP) [1]. Retinal degenerative diseases such as RP and age-related macular degeneration (AMD) have caused tens of millions of people to suffer varying degrees of irreversible vision loss. Many possible treatments are being explored and the artificial retina implant chip has been reported as a potential solution for patients that are blinded by RP or AMD [2], [3]. Several implementations of the implant chip have been reported. One method involves decoupling the photosensor and the stimulus electrode [4]–[6]. Image data and power are transmitted wirelessly from an external unit to the retinal implant. The other method, which we have adopted and reported in this paper, is where the image sensor and stimulus electrode array are located on the same chip while power is supplied wirelessly [7]–[9]. Yet another approach involves only passive devices whereby no external power is required [10].

It has been shown that spike trains, and not a constant amplitude stimulation, either electrically or optically, is the preferred method for eliciting response from the retinal cells [11]. Based on this fact, we are developing the subretinal implant chip based on the pulse-frequency modulation (PFM) photosensor circuit [7]. With the PFM photosensor, we can implement photosensitivity adaptation very much like that of the mammalian retina [12]. This has been demonstrated in our previous work [13]. Image processing based on the output pulse of the PFM circuit has been shown [14]. Also, we have verified that a thinned-down microelectronic chip, when bent to the curvature of the human eye, shows negligible change in circuit characteristics [15].

Manuscript received October 27, 2004; revised November 16, 2005. This work was partly supported by the "Artificial Vision System" project of the New Energy Development Organization (NEDO), Japan, and by the Health and Labor Sciences Research Grants, Japan. This paper was recommended by Associate Editor M. Soma.

The authors are with the Nara Institute of Science and Technology, Nara, 630-0101, Japan (e-mail: ohta@ms.naist.jp).

Digital Object Identifier 10.1109/TCSII.2006.875334

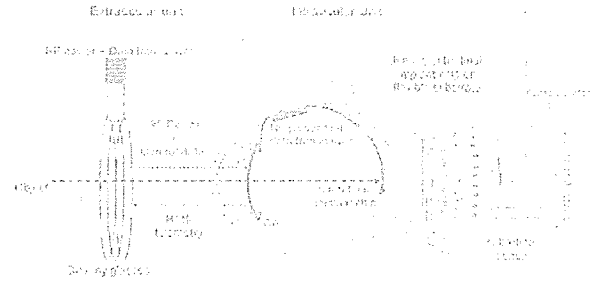

Fig. 1. Schematic of the proposed subretinal prosthesis system architecture. The extraocular unit provides power and interfaces wirelessly with the intraocular unit. The subretinal implant chip, which forms part of the intraocular unit, is surgically implanted in the space occupied by the dysfunctional photoreceptor cells.

The overall schematic of the retinal prosthesis system is shown in Fig. 1. Our aim is to develop a device that captures the image that falls onto the retina and deliver the necessary spatial and temporal electrical stimulus to the retina cells. To achieve this, we are developing the subretinal implant chip. With this chip, we have demonstrated digital pulse output images that are suitable for retinal cell stimulation. Electrical stimulation of the retinal cells is generated via a programmable waveform generator that controls the stimulus current in a linear and exponential fashion.

II. Subretinal Implant Chip

A. Design

The subretinal implant chip forms part of the intraocular unit shown in Fig. 2. The power receiver generates two voltage levels; a low of 3 and a high of 5 V. The lower regulated voltage is used to run the circuitry, including powering the embedded processor. In order to drive sufficient current through the high impedance electrode-cell interface it is necessary to operate the chip in active mode [7]–[9]. The higher voltage is used for this purpose. We implemented a dual voltage supply because, as the chip is scaled down to deeper submicrometer technology, the stimulus voltage can be fixed, independent of the circuitry voltage. This architecture will greatly ease future development in miniaturizing the chip. The embedded microprocessor generates the clock (CLK), reset (RST), and communication signals (RW, EXEC, SCLK, SDA) to the serial communication unit in the retinal implant chip.

The subretinal implant chip consists of the image sensing and stimulus block, and the control block. The current generator produces the necessary stimulus current to drive the stimulus electrodes located inside the pixel array. The register bank

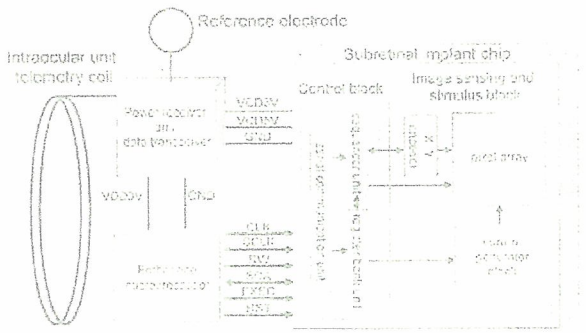

Fig. 2. Schematic of the intraocular unit. The power receiver supplies voltages to power the chip and for electrical stimulation. The embedded microprocessor communicates with the subretinal implant chip to set the various stimulus waveform parameters.

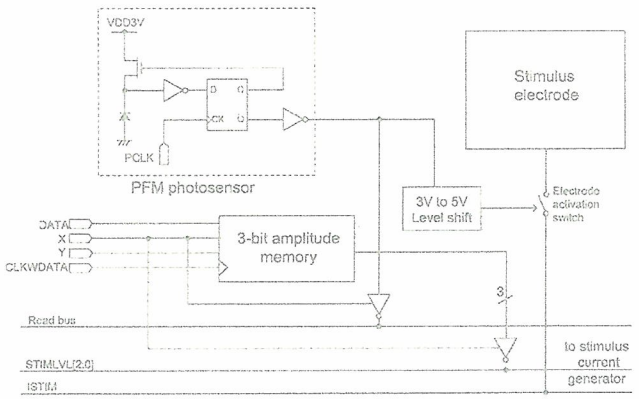

Fig. 3. Simplified schematic of the pixel showing the PFM photosensor circuit.

unit stores the various system memories for clock generation and stimulus waveform parameters. The sequencer unit generates timing clock signals. The serial communication unit clock (SCLK) running at 500 kHz enables data to be written or read to 10-bit address and data buffers.

A simplified schematic of the pixel circuit is shown in Fig. 3. It consists of the PFM photosensing circuit, a 3-bit stimulus amplitude memory, and a 100×100-μm^2 stimulus electrode. The stimulus amplitude level for each pixel is set independently using the DATA signal and latched to the 3-bit memory at the rising edge of the CLKWDATA signal.

B. Image Sensing

Image sensing is implemented using a 2-D array based on the PFM photosensor circuit. The PFM is a simple circuit that converts input light into output pulses with frequency varying in proportion to the light intensity [16], [17]. It can operate in either synchronous or asynchronous mode. We designed the image sensor for operation in the synchronous mode. This will ensure that at any time, only one pixel is active, thereby reducing power consumption when the output pulses activate the stimulus electrodes. Recently, it has been reported that operating in asynchronous mode, very wide dynamic range and low power consumption can be achieved [18]. However repeated firing of the electrodes in asynchronous mode may result in uncontrollable power consumption. Basically, the PFM circuit is a self-reset photodetecting circuit consisting of a comparator, a delay unit, and a reset switch. The comparator is implemented using an inverter. In the synchronous mode, the D flip-flop forces the

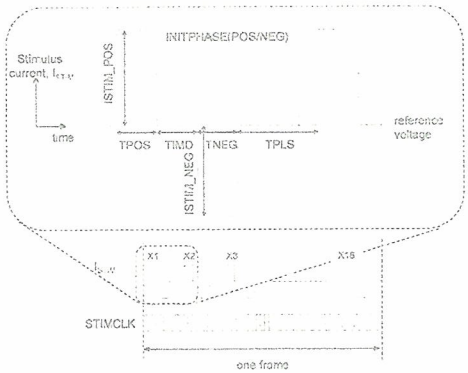

Fig. 4. Stimulus output waveform.

output of the PFM circuit to be synchronized to the input clock (PCLK), and also delay the feedback signal, rendering enough time for resetting the photodiode. The pulse output pulses from the PFM circuit are almost comparable to the electrical signal used for eliciting neural response from the human retina [2], [9]. Due to its digital-like output pulse, only simple signal post-processing is required to produce biphasic current stimulation. Also, because of its digital nature, it can be scaled down to deep-submicrometer process as these technologies become available.

C. Stimulus Current Generation

It has been shown that retinal cells respond differently when stimulated with either a negative or positive pulse first [2], [4]. Also, asymmetrical pulse (different phase amplitudes) has been reportedly used for retinal stimulation [19]. In order to cover the wide range of stimulation waveform requirements, we designed a programmable waveform generator. Seven parameters are used to define the stimulus waveform as shown in Fig. 4. The pulsewidth TPOS, TIMD, TNEG, and TPLS are 4-bit parameters each. The clock for generation of the pulse widths is STIMCLK. A frame is completed by scanning the column pixels using the X-decoder signal which also controls the tristate buffer output to STIMLVL[2:0]. Using a 2-MHz base clock, a typical operation scenario would be 1-ms pulsewidth resolution for the stimulus pulse running at about 100 Hz.

In order to reduce the necessary circuit area but still maintain a wide stimulus range with fine tuning resolution, we implemented a 3-bit linear and exponential digital–analog (D/A) conversion. The schematic for the current generator array is shown in Fig. 5. The current generator is designed using a series of current mirror circuit with varying transistor sizes. The stimulus current amplitude level is first read from a pre-assigned 3-bit memory in each pixel. This is then used to set the exponential amplifier driving current. The global 3-bit positive and negative phase current IOPOS[2 : 0] and IONEG[2 : 0] are used to tune the stimulus current to reach the desired value. The required current for stimulation IREF is generated from the current generator unit. This current is passed through the linear D/A converter (DAC) [Fig. 6(a)] where the 3-bit IOPOS[2 : 0] and IONEG[2 : 0] signal generates the reference voltages VREFPOS and VREFNEG, respectively. The linear DAC is implemented using a current source with three different transistor sizes. The reference voltage is then passed to the exponential DAC [Fig. 6(b)] where the 3-bit STIMLVL[2:0] signal, through a 3-bit decoder, controls the stimulus current in an exponential fashion. The stimulus current is powered by the higher

Fig. 5. Schematic of the stimulus current generator array block.

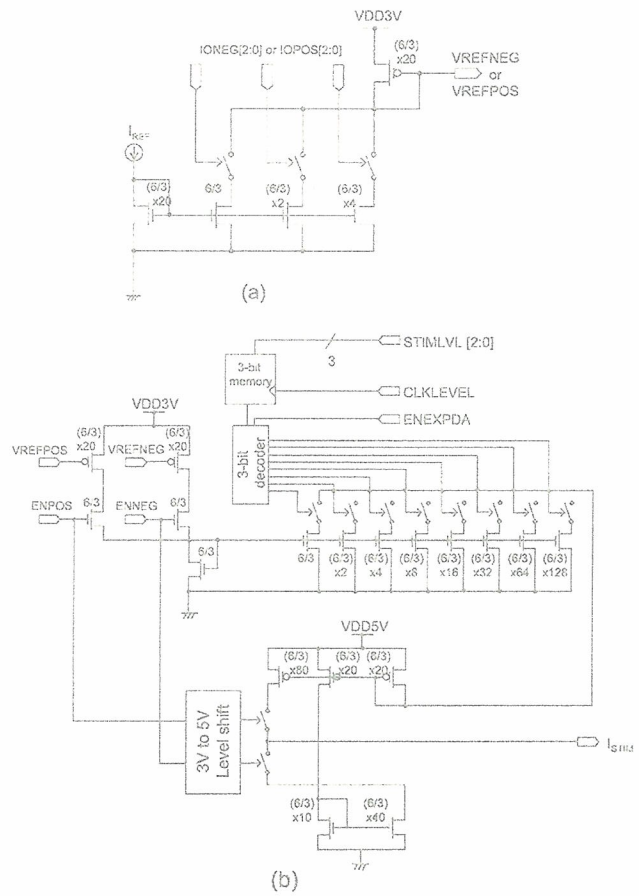

Fig. 6. Schematic of (a) linear D/A conversion, and (b) exponential D/A conversion. Numerator and denominator values refer to the width and length (in micrometers) of the transistor gates, respectively.

voltage source VDD5V. The final stimulus current can be described using the equation

$$I_{\mathrm{STIM}} = I_{\mathrm{REF}} \times \frac{IO}{20} \times 2^{\mathrm{STIMLVL}} \times 4 \qquad (1)$$

where IO is IOPOS when ISTIM is in the positive phase and IONEG when ISTIM is in the negative phase. This term represent the linearly increasing current. In order to reduce power consumption, current is generated only when pulses are

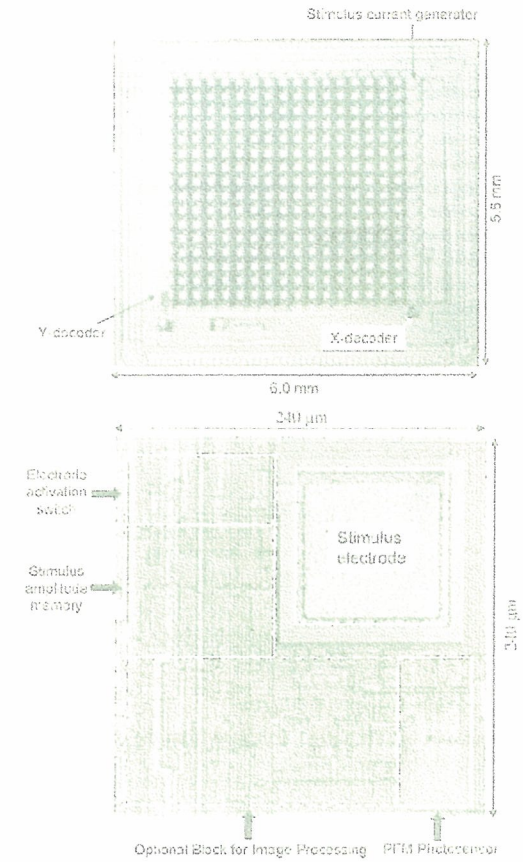

Fig. 7. Photomicrograph of the fabricated retinal implant chip. The enlarged view of the pixel is shown at the bottom.

required. This is controlled by the ENEXPDA signal, which enables the 3-bit exponential D/A conversion.

D. Control Block

It is necessary to generate the control signals and clocks, described above, to operate the retinal implant chip. Initially we opted for an off-chip solution. Eventually we will implement it as part of the chip. The register bank, sequencer, and serial communication unit in the control block were designed using behavioral modeling, written in Verilog HDL. Registers are needed for setting the clock frequencies, pulse parameters and image processing parameters. The various clock signals are generated from the base clock.

III. Measurement Results

The chip has been fabricated using standard 0.6-μm CMOS process. The microphotograph of the chip and the enlarged view of the pixel are shown in Fig. 7. The chip specification is listed in Table I.

In our experiment, the control block is implemented in FPGA (Altera Corp. Cyclone™ EPIC12Q240C8 on HuMANDATA Ltd. CSP-024D board) for fast debugging and code finalization. This generates the necessary control and timing signals for the stimulus array chip. The output stimulus output current is measured under a probe station. In order to visualize the output image from the chip, we measured the output pulses using a digital input board (Interface PCI-2772C). Fig. 8 shows a typical output of the pixel array. A backlit object illuminates

TABLE I
SPECIFICATION OF SUBRETINAL IMPLANT CHIP

Technology	0.6 μm CMOS (2-poly 3-metal)
Pixel count	16 x 16
Pixel size	240 μm x 240 μm
Frame rate	4 to 8,000 Hz
Voltage source	3 V (logic), 5 V (stimulus)
Base clock	2 MHz
Serial communication speed	500 kHz
Photodiode	n-well/p-substrate
Electrode size	100 μm x 100 μm
Amplitude resolution	3-bit exponential, 3-bit linear (biphasic)

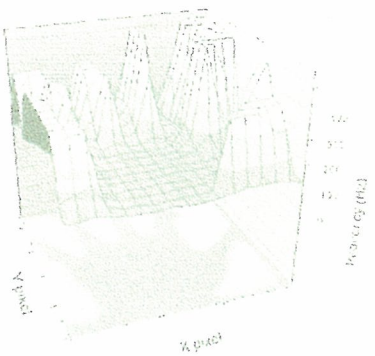

Fig. 8. Output of a backlit object visualized from the output pulse measurement.

the chip and the output pulses are measured. The region with high light intensity shows a corresponding high frequency pulse output while the region with low light intensity shows low frequency output. From the output we can clearly discern the image of a hand, which is used as the backlit object.

By using a current–voltage converter with 1000-V/A gain, we measured the stimulus current for both the zero load and loaded cases. In order to simulate the stimulus electrode driving a stimulus current through the retina cells, we used a cell filled with saline solution (0.155 M NaCl at pH6.4) and measured the current injected through the saline with a reference electrode placed around the stimulus electrode. The impedance of the cell at 1 kHz is about 80 kΩ. We have measured the exponential current increase by changing the 3-bit STIMLVL parameter. The result is shown in Fig. 9(a). The reference voltage is set to 2.5 V. At current values below 500 μA, the difference between the positive and negative phase output is less than 5% for the loaded case, which is fairly reasonable. Overall, the current source circuit could maintain a drive current for both the loaded and zero load cases, with a maximum difference of about 8%. The stimulus current saturates at about 500 μA (for both the positive and negative phase currents) corresponding to the maximum output voltage swing of 5 V, which is the supply voltage rail. Fig. 9(b) shows the linear biphasic current output. Combined, the linear and exponential incremental current values give a total of 64 current levels.

The stimulus current is measured by probing the stimulus electrode of the pixel. A typical output is shown in Fig. 10. There is some noise riding on the output current, but generally the output follows the set parameters fairly well. The output stimulus current waveform is fully re-configurable during operation by changing the register values of each of its parameters.

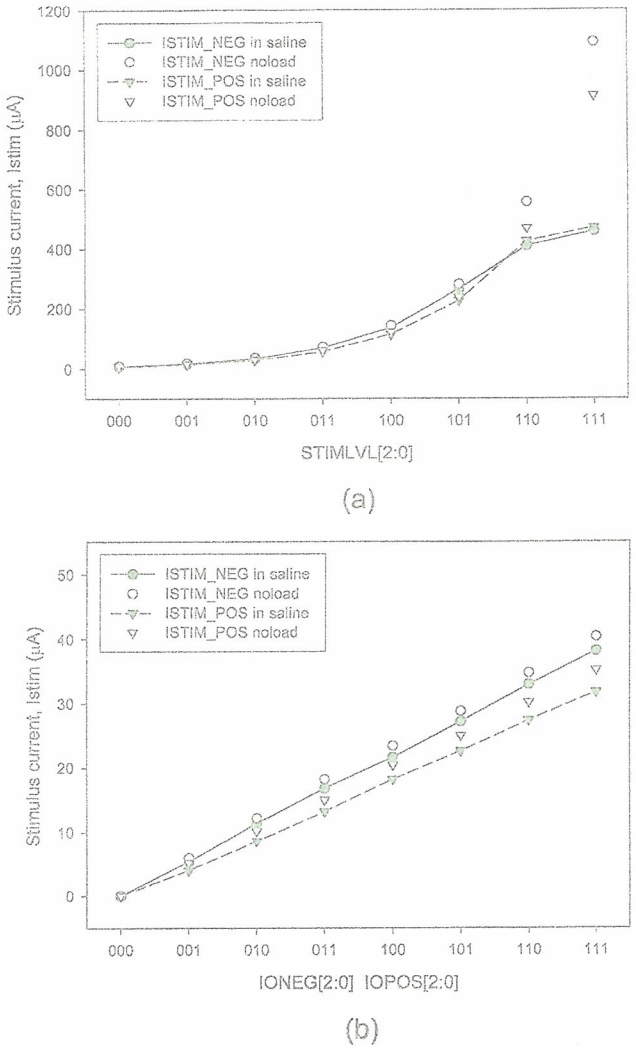

Fig. 9. (a) Exponential biphasic current amplifier output. (b) Linear biphasic current amplifier output.

IV. DISCUSSION

Although the optimal number of electrodes has yet to be established, it is argued that some 500 to 1000 pixels are needed to restore useful vision [4]. Due to the size of the stimulus electrodes, the number of pixels is limited by the size of the chip. We demonstrated that 16 × 16 pixels can sufficiently resolve basic shapes such as that of the hand.

There is a small discrepancy between the positive and negative phase pulse output currents. P- and N-channel MOSFETs are used for driving the positive and negative phase current respectively. Due to mismatch in transistor characteristics, the phase currents may not be equal. This mismatch, however, can easily be corrected by changing the various parameters in (1) to reach the desired output current level. In our experiment, we have substituted the subretinal space with a saline cell. The electrical resistance of the subretinal space is about 50 kΩ for an area of 0.01 mm^2 [20]. Therefore, usage of the saline cell in our experiment can be justified. Generally it is accepted that a stimulus threshold current of 100 μA, corresponding to a charge injection of 0.1 nC at a 0.1-ms interval, will illicit neuronal response from the retinal ganglion cells [2]. In the subretinal space, lower

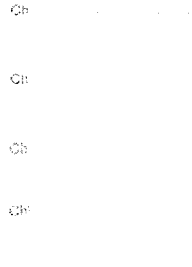

Fig. 10. Typical stimulus current output as measured on an oscilloscope. Ch1 and Ch2 are the ENPOS and ENNEG signal, respectively. Ch3 is the ENEXPDA, while Ch4 is the generated output current. The stimulus parameters are: IOPOS = IONEG = 5, TPOS = 1, TNEG = 2, TIMD = 0.

threshold current has been reported [11]. From the experimental results, we have achieved a higher than 500-μA stimulus current output. We have applied the chip in *in vitro* verification with a detached frog retina whereby, stimulus currents below 100 μA was confirmed to be able to evoke retinal response [21]. By using a special packaging technique which included fabrication of a stacked Pt/Au electrode on top of the stimulus electrode [22], the device was tested for stimulation inside the sclera of a rabbit for two weeks with no significant degradation in performance. The special electrode arrangement offered sufficient protection from electrode dissolution due to charge imbalances. Because the stimulus current is raster scanned one pixel at a time, the maximum power consumption of the device due to stimulus current alone is about 2 mW.

An electrode activation switch in the form of a CMOS transmission gate (Fig. 3) is connected to the stimulus electrode. The p-n junction area of the nMOS and pMOS at 94.5 and 189 μm^2, respectively, provided adequate ESD protection as no device failure due to ESD was encountered during testing.

In the future, we intend to reduce the size of the chip by using 0.35-μm CMOS process. Keeping the stimulus electrode area equal, we foresee a reduction of more than 50% for the pixel area. Also, the control block will be implemented on chip. The estimated size of the chip when fabricated using the new process is about 3 mm × 3 mm, subtending a visual field of 12°.

V. Conclusion

We have developed a CMOS image sensor chip for subretinal implantation based on the PFM photosensor circuit. Image sensing of sufficient resolution has been achieved from. A linear and exponentially controlled biphasic stimulus current exceeding the threshold levels of the human retina has also been demonstrated.

Acknowledgment

The authors thank Prof. Y. Tano and Prof. T. Fujikado, and K. Nakauchi, MD for their feedback and support on the semichronical in vivo experiments.

References

[1] J. R. Heckenlively, , J. R. Heckenlively, Ed., "The diagnosis and classification of retinitis pigmentosa," in *Retinitis Pigmentosa*. Philadelphia, PA: JB Lippincott, 1988, pp. 21–23.

[2] E. Margalit, M. Maia, J. D. Weiland, R. J. Greenberg, G. Y. Fujii, G. Torres, D. V. Piyathaisere, T. M. O'Hearn, W. Liu, G. Lazzi, G. Dagnelie, D. A. Scribner, E. de Juan, Jr, and M. S. Humayun, "Retinal prosthesis for the blind," *Surv. Ophthalmol.*, vol. 47, pp. 335–356, Jul. 2002.

[3] E. Zrenner, "Will retinal implants restore vision?," *Science*, vol. 295, pp. 1022–1025, Feb. 2002.

[4] M. S. Humayun, E. de Juan Jr., J. D. Weiland, G. Dagnelie, S. Katona, R. Greenberg, and S. Suzuki, "Pattern electrical stimulation of the human retina," *Vision Res.*, vol. 39, pp. 2569–2576, Jul. 1999.

[5] M. Schwarz, R. Hauschild, B. J. Hosticka, J. Huppertz, T. Kneip, S. Kolnsberg, L. Ewe, and H. K. Trieu, "Single-chip CMOS image sensors for a retina implant system," *IEEE Trans. Circuits Syst. II, Analog Digit. Signal Process.*, vol. 46, pp. 870–877, Jul. 1999.

[6] W. Liu, K. Vichienchom, M. Clements, S. C. DeMarco, C. Hughes, E. McGucken, M. S. Humayun, E. de Juan, J. D. Weiland, and R. Greenberg, "A neuro-stimulus chip with telemetry unit for retinal prosthetic device," *IEEE J. Solid-State Circuits*, vol. 35, no. 10, pp. 1487–1497, Oct. 2000.

[7] J. Ohta, N. Yoshida, K. Kagawa, and M. Nunoshita, "Proposal of application of pulsed vision chip for retinal prosthesis," *Jpn. J. Appl. Phys.*, vol. 41, pp. 2322–2325, Apr. 2002.

[8] A. Dollberg, H. G. Graf, B. Höfflinger, W. Nisch, J. D. S. Spuentrup, K. Schumacher, and E. Zrenner, "A fully testable retinal implant," in *Proc. BioMED*, Jun. 2003, pp. 255–260.

[9] D. Ziegler, P. Linderholm, M. Mazza, S. Ferazzutti, D. Bertrand, A. M. Ionescu, and P. Renaud, "An active microphotodiode array of oscillating pixels for retinal stimulation," *Sens. Actuators A*, vol. 110, pp. 11–17, 2004.

[10] A. Y. Chow, M. T. Pardue, V. Y. Chow, G. A. Peyman, C. Liang, J. I. Perlman, and N. S. Peachey, "Implantation of silicon chip microphotodiode arrays into the cat subretinal space," *IEEE Trans. Neural Syst. Rehab. Eng.*, vol. 9, no. 1, pp. 86–95, Mar. 2001.

[11] A. Stett, W. Barth, S. Weiss, H. Haemmerle, and E. Zrenner, "Electrical multisite stimulation of the isolated chicken retina," *Vision Res.*, vol. 40, pp. 1785–1795, Jun. 2000.

[12] B. Sakmann and O. D. Creutzfeldt, "Scotopic and mesopic light adaptation in cat's retina," *Pflugers Arch.*, vol. 313, pp. 168–185, 1969.

[13] K. Kagawa, K. Isakari, T. Furumiya, A. Uehara, T. Tkuda, J. Ohta, and M. Nunoshita, "Pixel design of a pulsed CMOS image sensor for retinal prosthesis with digital photosensitivity control," *Electron. Lett.*, vol. 39, pp. 419–421, Mar. 2003.

[14] K. Kagawa, K. Yasuoka, D. C. Ng, T. Furumiya, T. Tokuda, J. Ohta, and M. Nunoshita, "Pulse-domain digital image processing for vision chips applicable to low-voltage operation in deep-submicron technologies," *IEEE J. Select. Topics Quantum Electron.*, vol. 10, no. 7, pp. 816–828, Jul. 2004.

[15] D. C. Ng, K. Isakari, A. Uehara, K. Kagawa, T. Tokuda, J. Ohta, and M. Nunoshita, "A study of bending effect on pulse-frequency-modulation-based photosensor for retinal prosthesis," *Jpn. J. Appl. Phys.*, vol. 42, pp. 7621–7624, Dec. 2003.

[16] W. Yang, "A wide-dynamic-range, low power photosensor array," in *Dig. Tech. Papers IEEE ISSCC*, 1994, pp. 230–231.

[17] F. Andoh, H. Shimamoto, and Y. Fujita, "A digital pixel sensor for real-time readout," *IEEE Trans. Electron Devices*, vol. 47, pp. 2123–2127, 2000.

[18] E. Culurciello, R. Etienne-Cummings, and K. A. Boahen, "A biomorphic digital image sensor," *IEEE J. Solid-State Circuits*, vol. 38, no. 1, pp. 281–294, Jan. 2004.

[19] M. N. Nadig, "Development of a silicon retinal implant: Cortical evoked potentials following focal stimulation of the rabbit retina with light and electricity," *Clin. Neurophysiol.*, vol. 100, pp. 1545–1553, 1999.

[20] C. J. Karwoski, D. A. Frambach, and L. M. Proenza, "Laminar profile of resistivity in frog retina," *J. Neurophysiol.*, vol. 54, pp. 1607–1619, 1985.

[21] T. Furumiya, D. C. Ng, K. Yasuoka, K. Kagawa, T. Tokuda, M. Nunoshita, and J. Ohta, "Functional verification of pulse frequency modulation-based image sensor for retinal prosthesis by *in vitro* electrophysiological experiments using frog retina," *Biosens. Bioelectron.*, vol. 21, pp. 1059–1068, Jan. 2006.

[22] T. Tokuda, Y.-L. Pan, A. Uehara, K. Kagawa, M. Nunoshita, and J. Ohta, "Flexible and extendible neural interface device based on cooperative multi-chip CMOS LSI architecture," *Sens. Actuators A*, vol. 122, pp. 88–98, Mar. 2005.

©EYEWIRE

A Flexible and Extendable Microchip-Based Stimulator

BY JUN OHTA, TAKASHI TOKUDA, KEIICHIRO KAGAWA, TETSUO FURUMIYA, AKIHIRO UEHARA, YASUO TERASAWA, MOTOKI OZAWA, TAKASHI FUJIKADO, AND YASUO TANO

Neural electronic stimulators play an important role in neuroscience and clinical neuroengineering. Stimulators are now commercially available, while others continue to be developed [1]–[11]. As examples in clinical neuroengineering, stimulators have been applied to cochlear prostheses [12], [13] and retinal prostheses [14]–[20]. In this article, we focus on retinal prosthesis as schematically shown in Figure 1. In the configuration, the implanted stimulator is placed upon the suprachoroid; this stimulation method is called STS (suprachoroidal transretinal stimulation) [21], [22].

The stimulator includes several electrodes that stimulate the retinal cells electrically and evoke a spatial phosphen pattern. Thus, the number of the electrodes is considered to be important, although at the present time, only a small number of stimulus electrodes have been realized. Creating devices with over 1,000 electrodes is challenging; such a large number of connections between electrodes and external lead wires are extremely difficult to fabricate.

Recently, neural interface devices based on silicon microelectronics or large-scale-integration (LSI) have emerged [23]–[38]. Since LSI allows the integration of smart functions such as control, amplification, and signal processing with the stimulators, LSI-based neural interface devices are attracting significant interest. To solve the interconnection issue, we have proposed the introduction of LSI technologies to retinal prosthesis devices [39]–[48]. In addition to solving the interconnections issue, LSI-based stimulators bring several advantages to photosensors for subretinal implantation. We have studied LSI-based stimulators for STS [47], [48], subretinal implantation [39]–[44], and epiretinal implantation [45].

There are many technical challenges to overcome when applying LSI-based neural interface devices to retinal prosthesis. First, the LSI-based interface must be biocompatible. A standard LSI structure is not at all suitable in a biological environment; silicon nitride is conventionally used as a protective top layer in standard LSIs but is eroded in a biological environment. Second, the stimulus electrodes must be compatible with the standard LSI structure; aluminum is conventionally used for wire-bonding pads in standard LSIs but is completely inadequate as a stimulus electrode for neural cells because aluminum dissolves in saline solution. Third, in addition to the electrode material, the shape of the electrode affects the efficiency of stimulation, with a convex shape being suitable for efficient stimulation. Consequently, we need to develop a completely new packaging technology that fits into a standard LSI structure, is biocompatible, and is effective in stimulating neural cells. Finally, the devices must also be thin and flexible to fit the anatomy of target organs and to avoid damaging tissues. However, silicon, the base material of the LSI chip, is so rigid that thinning of the LSI chip increases the risk of breakage. We have previously demonstrated that an image sensor made of silicon thinner than 50 μm can be bent and can operate with sufficient accuracy [41]. Such a thinned LSI chip, however, must be handled very carefully. To overcome the issue of mechanical rigidity and to realize a feasible LSI-based neural interface device, we have proposed a device architecture consisting of silicon (Si)-based microchips that cooperatively operate under a single set of control signals [46]–[48].

In this article, we report on a retinal prosthesis smart stimulator that is biocompatible and fully compatible with a standard LSI structure and that provides high-stimulation efficiency. Our stimulator is based on multimicrochip architecture. We have specifically developed the stimulator for retinal prostheses, but it could be applied to other neuroscience and clinical neuroengineering fields.

Si-LSI Based Stimulator: Operation Principle and Fundamental Characteristics

Circuit Design Issues

To stimulate retinal cells effectively, biphasic current pulse stimulation is generally preferred [49]. In addition, biphasic pulses are required to maintain the charge balance of the biological environment [50]. When such stimulation is implemented using standard LSI technology, a necessary consideration is that the output current and voltage range must stay within the limits of the technology. That is, the output current must stay within about -500 to $+500\,\mu$A and the voltage from slightly below 0 V to the power supply voltage V_{dd} of the LSI technology used; for example, using standard 0.6-μm CMOS (complementary metal oxide semiconductor) technology, the range is from -0.5 to $+5.5$ V. It is noted that when we use a biphasic current pulse, the reference voltage

0739-5175/06/$20.00©2006IEEE

We need to develop a completely new packaging technology that fits into a standard LSI structure, is biocompatible, and is effective in stimulating neural cells.

V_{ref} is usually set at half of the full swing of voltage range in the system used, and, therefore, the voltage swing in one polarity must be less than $0.5 \times V_{dd}$. For example, for $V_{dd} = 5$ V, the positive voltage swing must be less than 2.5 V. Consequently, it is necessary to design an LSI that can output enough high pulse current amplitude in the voltage range in a biological environment such as saline solution.

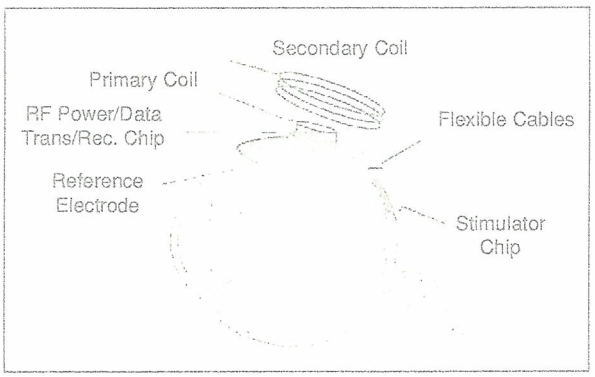

Fig. 1. The conceptual drawing of a retinal prosthesis. The implanted chip is placed upon the suprachoroid in this case (47).

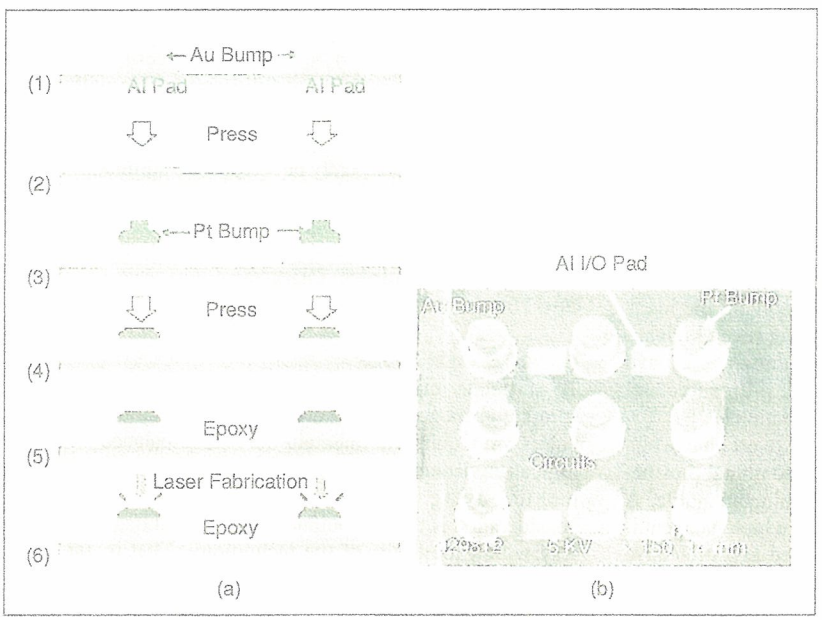

Fig. 2. Pt/Au stacked bump electrodes on an LSI chip. (a) Fabrication process flow: (1) gold bump forming, (2) pressing of gold bump, (3) platinum bump forming, (4) pressing of platinum bump, (5) molding, and (6) platinum exposure. (b) SEM photograph (48).

Electrodes and Packaging

The electrodes and packaging technologies used in the design of a standard LSI-based stimulator are now described. Figure 2(a) shows the fabrication process for our electrode [47], [48]. First, a platinum/gold (Pt/Au) stacked bump structure is formed on an aluminum (Al)-bonding pad in a standard LSI chip. Aluminum cannot be used in the biological environment, but platinum is a suitable electrode material due to its excellent biocompatibility and charge injection efficiency [51]–[53]. The platinum electrode juts out of the top surface of the chip to enable close contact with neural cells. To make this jutting platinum electrode, we have formed the stacked bump in two steps, in which a gold bump is initially formed and a platinum bump is formed on top. The gold bump acts as a cushion for the hard platinum bump; direct formation of the platinum bump sometimes breaks the LSI I/O pad.

After fabrication of the stacked Pt/Au bump, the entire LSI chip, including the bonding wires, is covered with a biocompatible epoxy resin. Finally, the resin on top of the electrodes is completely removed using a high-power argon (Ar) ion laser; thus the entire LSI chip, except for the top of the platinum electrodes, is covered with resin. Parylene coating can be additionally applied to the resin to ensure durability in the biological environment and can also be removed by the Ar ion laser.

Figure 2(b) shows a scanning electron micrograph (SEM) of the stacked Pt/Au bump electrodes fabricated on an LSI chip. The diameter of the structure is about 100 μm and can be controlled by changing the silver and platinum wire diameter. We have obtained good reproducibility in fabricating over 100 such bump electrodes using an automatic bump bonder. The coating has been confirmed to protect the interior of the LSI chip, including the area close to the electrodes, from the biological environment. It is noted that other high-efficiency, biocompatible electrode materials such as iridium oxide (IrO_x) and titanium nitride (TiN) [54], [55] can be deposited on the platinum bump.

Operation in Saline Solution

To assess the applicability of the electrodes and packaging technologies, we operated the fabricated stimulator in a saline environment. The stimulator

Our smart LSI-based stimulator is effective in stimulating retinal cells.

chip was fabricated in 0.6-μm standard CMOS technology. The chip formed with a Pt/Au stacked bump electrode was wire-bonded to a test board and was molded. Then the coating on the platinum electrode was removed by an excimer laser to leave an exposed area with a diameter of about 20 μm, by the process described above. A reservoir of saline solution was formed around the chip. Figure 3(a) shows the processed chip on the test board with the reservoir. The details of the circuits are described in a later section.

The molded chip was dipped in saline solution and the reference voltage $V_{ref} = 1.5$ V was supplied via an silver/silver chloride (Ag/AgCl) reference electrode. The biphasic pulse parameters are the amplitudes of the cathodic and anodic currents, I_c and I_a, and the pulse durations of the anodic, cathodic, and interpulses, t_c, t_i, and t_a. In this work, we fixed $|I_c| = I_a$. The pulse durations t_c, t_i, and t_a were set to the same value. Hence, the biphasic pulse waveform can simply be described by the amplitude and interval, for example, 100 μA/100 μs.

Figure 3(b) shows the measured operational voltage for three biphasic, current-controlled pulses. The pulse parameters used are shown in the figure. Similar reports on neural stimulation using platinum electrodes suggest that the trace presented in Figure 3(b) is reasonable for a cathodic-first biphasic charge injection [51], [52]. In Figure 3(b), the operational voltage lies within the voltage swing of the chip (from −0.5 to +5.5 V for the present device) for typical conditions in retinal cell stimulation experiments. This indicates that the LSI chip can output sufficient biphasic current pulses to stimulate retinal cells.

Another consideration relates to the electrochemical aspect of current injection into a biological environment. Current injection from an electrode into saline (or other biological solution) includes electrochemical reactions at the interface. Excess voltages applied to the interface cause irreversible chemical reactions such as electrolysis and the formation of bubbles [52], [53]. The current injection for neural stimulation needs to be carried out without causing irreversible electrolysis or bubbles. The current injection capability depends on the material and surface structure of the electrode. In our experiments, we have confirmed in electrochemical experiments using platinum electrodes that the voltage for appropriate current injection swings within the safe range for reversible electrochemical processes. In addition, we observed no bubbles on the platinum electrodes during current injection. Consequently, we conclude that the present packaging of Pt/Au stacked bump electrodes is applicable for neural stimulation.

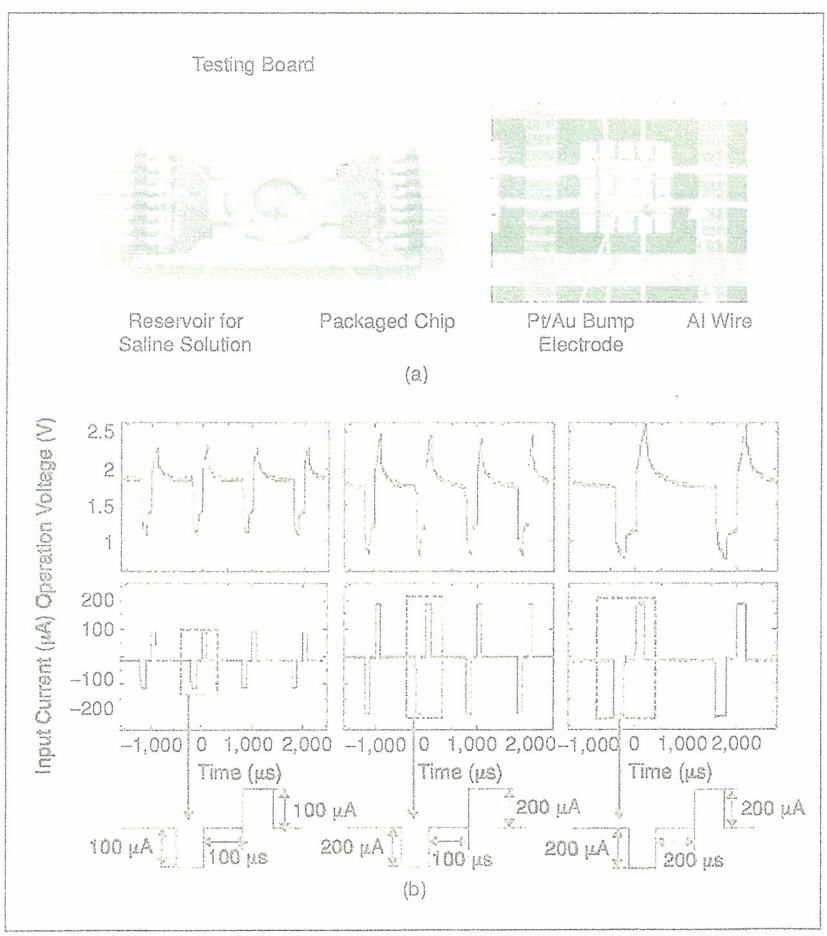

Fig. 3. Current injection experiments of Pt/Au stacked bump electrodes in a saline environment (48). (a) A packaged LSI chip on a testing board for experiments in a saline environment. (b) Oscilloscope traces of current stimulation in a saline solution. Upper and lower traces show voltages of electrodes and injection current, respectively.

Stimulation of Frog Retina with a Smart LSI-Based Stimulator

Electrical Stimulation Using a Smart LSI-Based Stimulator

In the previous section, we demonstrated the successful operation of the LSI stimulator in saline solution. In this section, we show that our smart LSI-based stimulator is effective in stimulating retinal cells. We used detached bullfrog retinas as the in vitro experiment [44]. The stimulator used was a CMOS image sensor-based stimulator array we have developed for retinal prostheses [43], [44]. Table 1 summarizes the chip specifications.

Table 1. Chip specifications.

Technology		0.6 μm standard 2-poly 3-metal CMOS
Number of pixels		16 × 16
Pixel size		240 μm × 240 μm
Power supply voltage		3 V (logic), 5 V (stimulus)
Stimulus electrode size		About 100 μm ϕ
Stimulus current	Range	−1 to +1 mA (biphasic)
	Resolution	exponent: 3-b; significand: 3-b

The chip has two functions, which can be switched; an externally controlled stimulator and a stimulator that is controlled by input light intensity such as in photoreceptor cells. A current source and pulse shape circuits are integrated on the chip (the details are described in [43], [44]). The Pt/Au stacked bump electrode and chip molding processes were performed as described in the previous section. Before molding, the chip was bonded onto a printed circuit board for handling. A reservoir of Ringer solution was placed surrounding the chip.

A piece of the bullfrog retina (about 3–5 mm in width) was placed, with the retinal ganglion cell (RGC) side face up, on the surface of the packaged chip. Figure 4(a) shows the experimental setup. Electrical stimulation was performed using the chip at a selected single pixel. A tungsten counter electrode with a tip diameter of 5 μm was placed on the retina and, thus, a transretinal current was produced between the counter electrode and the chip electrode. A top-view photograph of

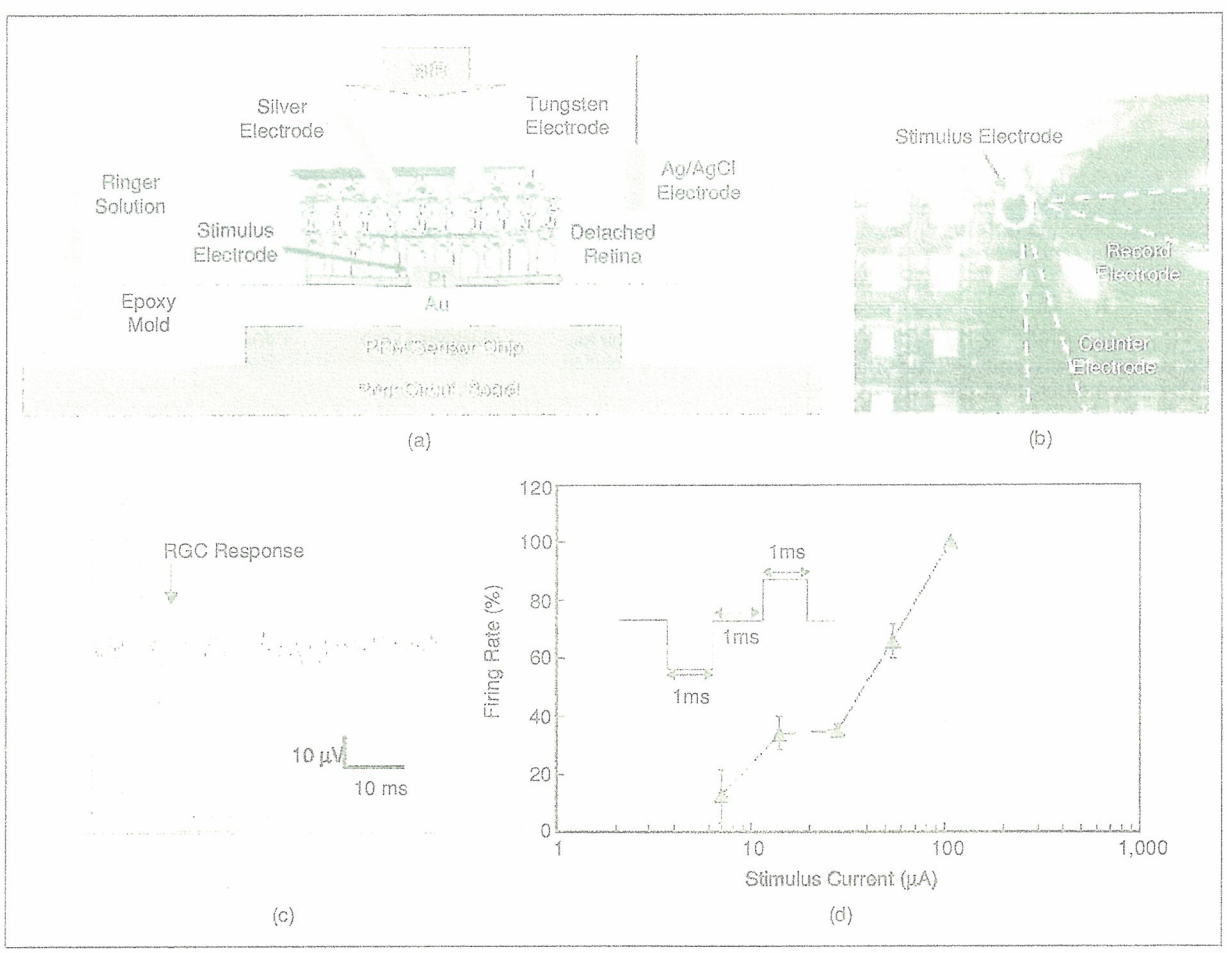

Fig. 4. The electrical stimulation of a detached retina with the fabricated LSI-based stimulator (44). (a) Experimental setup, (b) a microphotograph of the experiment, (c) an example of the RGC response waveform, and (d) the firing rate of the RGC as a function of the stimulus pulse amplitude.

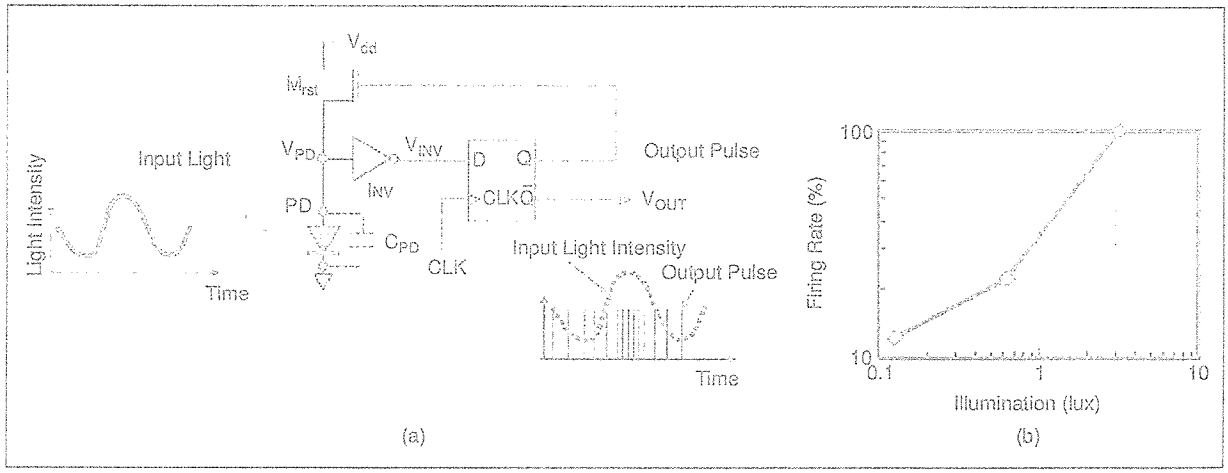

Fig. 5. Light-to-pulse stimulation: (a) the schematic of a PFM photosensor and (b) the firing rate of RGCs as a function of the input NIR light intensity (44).

the experimental setup is shown in Figure 4(b). We used a cathodic-first biphasic current pulse. Stimulus pulses were generated with the chip for $t_c = t_i = t_a = 1$ ms and $I_a = |I_c|$. A silver electrode with a diameter of 50 μm was used to record the extracellular response of the RGCs. An Ag/AgCl wire was used for the reference electrode.

We have previously examined the firing rate of the RGC response [44]; Figure 4(c) shows an example of the RGC response waveform obtained. We have confirmed that the firing rate increases in response to input light intensity as shown in Figure 4(d). This demonstrates the effectiveness of the developed electrodes, which are compatible with the standard LSI structure.

Light-to-Pulse Stimulation

The chip is integrated with an image sensing function; that is, the input light intensity is converted into pulse trains with the pulse frequency proportional to the input light intensity. This device, known as a *pulse-frequency-modulation (PFM) photosensor* [56], is suitable for stimulating retinal cells. We were the first to propose that a PFM-based photosensor could be applied to a retinal prosthesis device [39]. The schematic of a PFM photosensor is shown in Figure 5(a). The operation principle is briefly described as follows. The node voltage V_{PD} decreases by discharging the parasitic capacitance C_{PD} through the photocurrent, and eventually, when V_{PD} reaches the threshold voltage of the inverter V_{th}, the inverter turns on, resets the transistor M_{rst}, and finally charges C_{PD}, which is the initial state. The D-FF (flip-flop) acts as a delay element. The pulse is output when the inverter chain turns on and results in a pulse frequency that is proportional to the input light intensity. We have already fabricated and demonstrated PFM photosensors [39]–[41] and have analyzed their operation theoretically [42]. Such a photosensor could be applied to subretinal implantation and has been recently studied by other researchers [57].

Subsequently, we have tested this PFM function in stimulation of the detached frog retina. The experimental setup is the same as for electrical stimulation except for an additional input of near-infrared (NIR) light. Note that NIR light

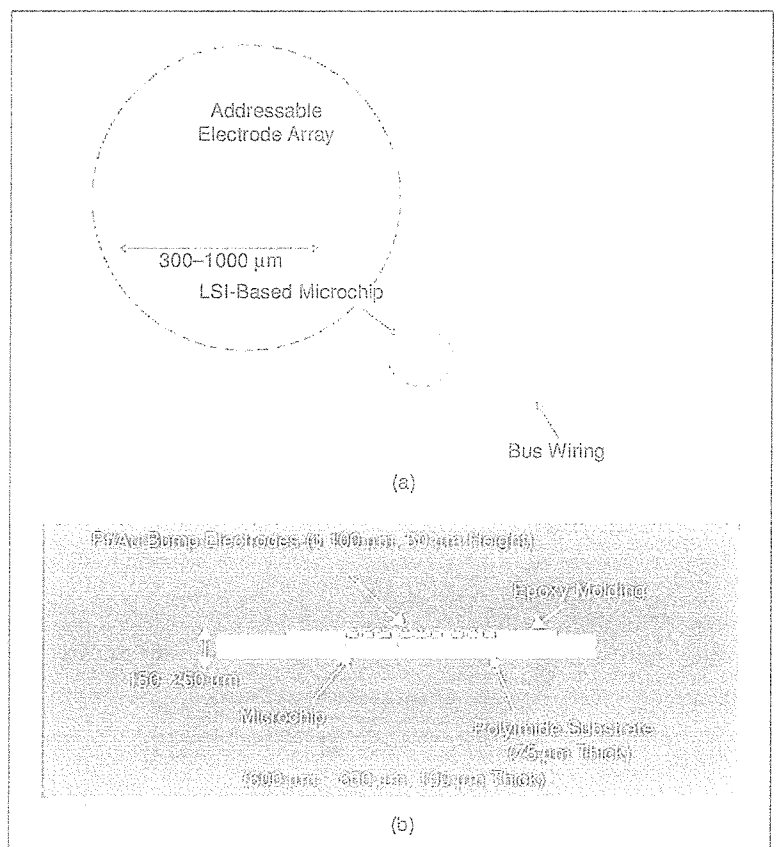

Fig. 6. A conceptual drawing of the smart distributed LSI-based microchip array (4). Each microchip has stimulus electrodes: (a) a schematic of the entire array and (b) a cross-sectional view.

To implant the device with a minimum of difficulties, the thickness of the device must be as thin as possible.

does not excite the retinal cells but does excite the PFM photosensor cells. We have confirmed that the firing rate increases as the input NIR light intensity increases. This demonstrates that the smart LSI-based stimulator activates the retinal cells through an input of NIR light and suggests that it could be applied to human retinal prosthesis. Figure 5(b) shows the dependence on the input NIR light intensity and clearly indicates that the firing rate increases in relation to the input light intensity. This in vitro experiment suggests the effectiveness of the PFM photosensor for a stimulator device in subretinal implantation.

The Microchip-Based Smart Stimulator

In the previous sections, we have demonstrated a smart LSI-based neural stimulator. To apply the device to a retinal prosthesis, however, it must be implanted in the eyeball and will inevitably be bent. As already mentioned, a thinned Si-LSI chip is fragile. Another issue arises associated with fragility; that is, how to realize a large number of electrodes using Si-LSI. For example, a 1,000-electrode array needs an area of over 10-mm^2, and the fragile characteristics of Si prevent such a large chip size. Thus, flexibility and extendibility are issues to be solved for the implementation of a Si-LSI stimulator as a retinal prosthesis device.

In this section, we propose and demonstrate a solution to the flexibility and extendibility limitations of our smart LSI-based stimulator. We have developed a new type of smart stimulator that consists of a number of microchips distributed on a flexible substrate. Figure 6 shows the concept and cross-sectional view of our smart distributed stimulator. The array consists of a number of LSI-based microchips, each of which is about 500-μm square. Each microchip has several Pt/Au stacked bump electrodes and is covered by the same process as described previously. We have developed two types of architecture for the microchip-based stimulator: broadcast and serial bus. The broadcast architecture is simple but only stimulates one electrode at a time, while the serial bus architecture consumes a large area for circuitry but stimulates multiple electrodes.

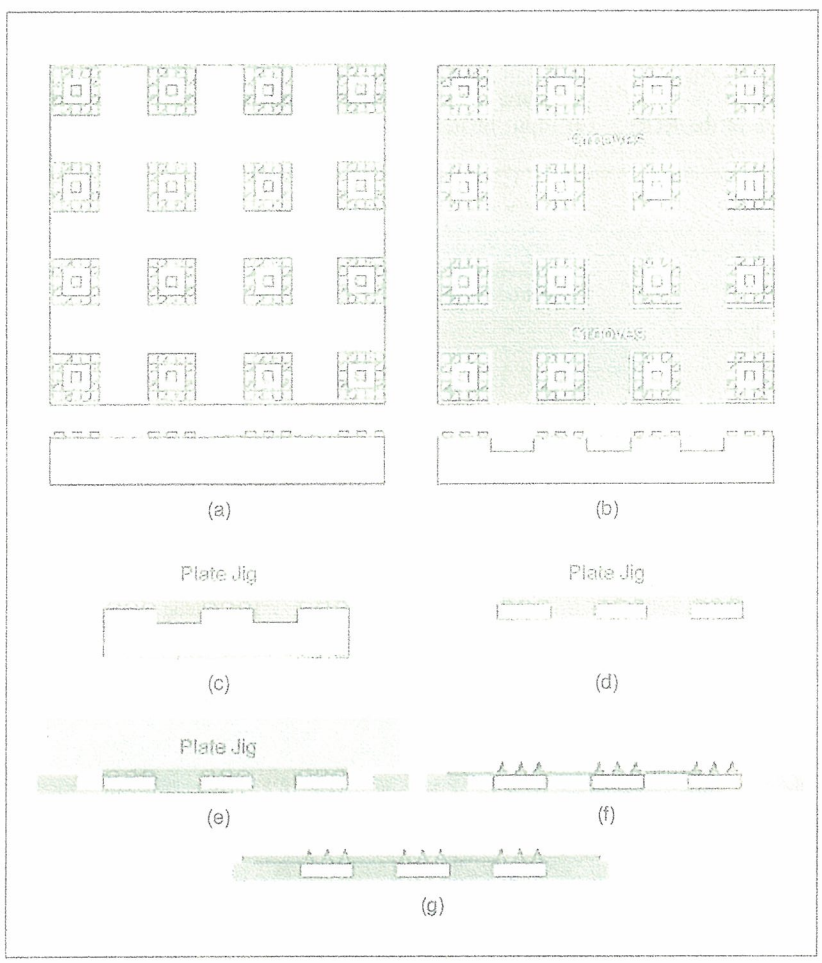

Fig. 7. The process flow of fabrication of the microchip-based stimulator (47). (a) bare die (4 × 4 microchips), (b) groove formation, (c) gluing wax onto a flat jig, (d) back-grinding and separation, (e) gluing onto a flexible substrate (thermal removal of jig), (f) wiring and bump forming, and (g) molding with epoxy resin.

The Fabrication Process of Microchip-Based Smart Stimulator

For the smart distributed microchip architecture, we have developed a dedicated fabrication process. Figure 7 illustrates the process flow. The "mother" chip contains several of the microchips. In the mother chip, grooves over 100-μm deep are formed around the microchips by micromachining using an excimer laser. The chip is bonded upside-down to a plate jig with wax and is then thinned to a thickness

of 50–100 μm. Finally, the chip is bonded to a flexible polyimide substrate with thermosetting epoxy resin. The plate jig is automatically removed. The Pt/Au stacked bump electrodes and coating process are the same as previously described.

The fabricated stimulator is shown in Figure 8. To implant the device with a minimum of difficulties, the thickness of the device must be as thin as possible; our device has a thickness of around 200 μm, which is acceptable. As shown in Figure 8(b), the device can be bent easily. An image of the entire stimulator with platinum wires covered with silicone tubing is shown in Figure 8(c). The width of the stimulator is about 3 mm.

In order to validate the stimulator in semichronic implantation, we have fabricated a stimulator by the same process described above except, in this case, the microchip is just a silicon substrate with a single Pt/Au bump electrode formed on it. The stimulator was implanted in the sclera pocket of a rabbit, and the electrically evoked potential (EEP) with stimulating retinal cells was measured daily. After two weeks, the EEP signal slightly decreased but was measurable. These results demonstrate the possibility of applying the stimulator to retinal prostheses, although further studies are required to investigate long-term biocompatibility, safety, and other factors.

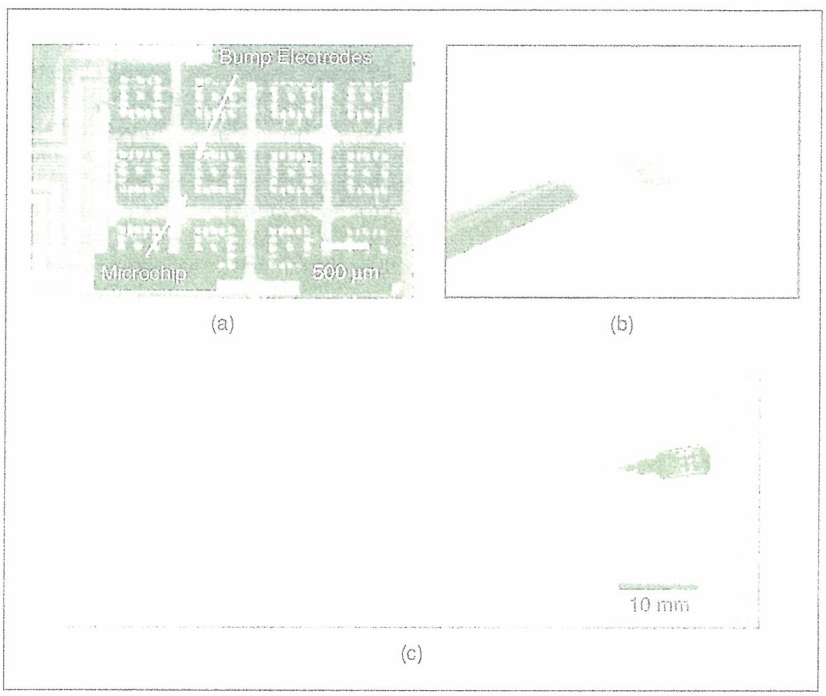

Fig. 8. Photographs of the fabricated microchip-based stimulator (47): (a) close-up of the microchips, (b) bending of the stimulator, and (c) the stimulator with platinum wires covered with silicone tubing.

A Smart Distributed Stimulator with Broadcast Architecture

In the stimulator with broadcast architecture, the microchips are connected to each other via two wires (not including the power supply lines) and are placed on a flexible polyimide substrate. The features of the new chip are as follows. First, it is thin and bendable so that it can achieve closer contact with neural cells when implanted and, thus, is suitable for stimulating neural cells. Second, the incorporation of LSI in the microchip allows control and processing of the signals; for

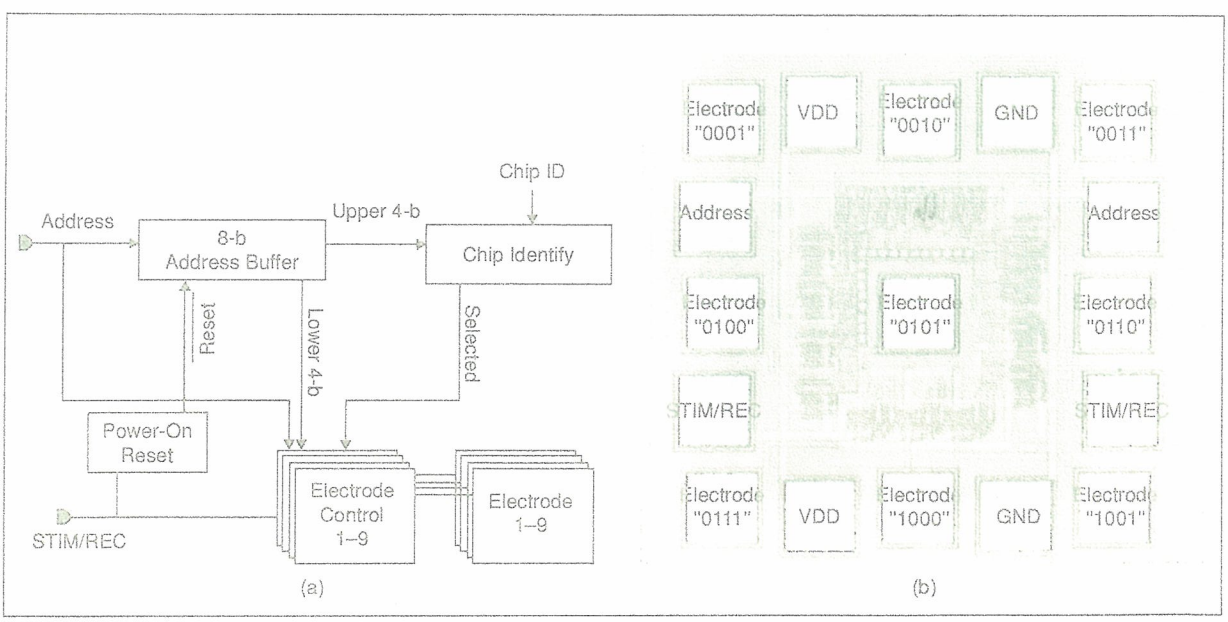

Fig. 9. (a) The circuit diagram and (b) layout of the microchip with broadcast architecture (48).

The application of LSI technologies confers benefits such as versatility, signal integrity, and compactness.

example, on-chip amplification circuitry enhances the signal-to-noise ratio in the monitoring of the electrode impedance, and both sensing and detecting can be implemented on the same chip. This provides the device with high performance and versatility. In addition, LSI reduces the input/output pads needed in the device such that only two signal lines for stimulation/record and control are required apart from the power supply lines. The control line operates the entire set of microchips, and each microchip includes enough circuitry to decode the control signal. Third, the device can be connected with another device; such a "daisy chain" could combine a large number of electrodes, for example, over 1,000 electrodes.

Figure 9 shows the circuit block diagram and the layout of the microchip [44], [45]. The chip is fabricated using 0.6-μm 2-poly 3-metal standard CMOS technology. The microchip is so small, at 600 μm × 600 μm, that it can be thinned down to less than 100 μm without risk of it breaking, as shown in Figure 8(b). The fabricated microchip has nine stimulation/recording electrodes and control circuits with four input/output (I/O) pads for addressing (ADDRESS) and stimulation/recording (STIM/REC) and four pads for power supply (VDD and GND), as shown in Figure 10. It is to be noted that each microchip relays ADDRESS and STIM/REC lines in the vertical direction and VDD and GND lines in the horizontal direction (Figure 10). This wiring architecture reduces the wiring area on the substrate.

We use a broadcast topology to assign one electrode to be activated; this consumes only a small area of circuitry, sufficiently small for the size of the microchip. An external controller broadcasts a control signal to all of the microchips. Each microchip has its own identification tag (ID). The microchip has an 8-b asynchronous counter as an address buffer [see Figure 9(a)]. The addressing counter counts the digital pulses applied to the ADDRESS line, and the microchip interprets the value in the counter as the address of the selected electrode. The upper 4 b and the lower 4 b represent the addresses of the selected chip and the selected electrode, respectively. Only the selected electrode on the selected chip is connected to the STIM/REC line. Once selected, neural stimulation/recording can be activated at the selected electrode via the STIM/REC line. The ID of each microchip is shown in Figure 10(a). Figure 10(b) shows experimental results of the fabricated stimulator in a saline solution. In each timing, only one electrode is activated, thus demonstrating that an arbitrary electrode can be selectively activated.

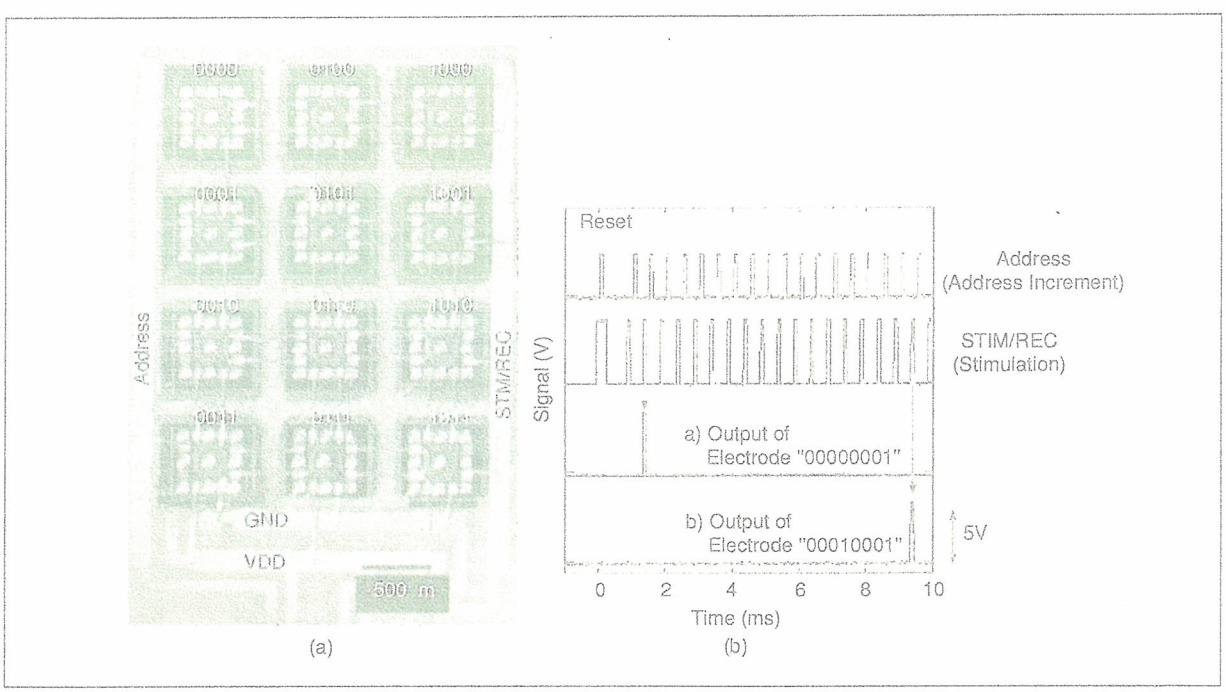

Fig. 10. (a) Connection diagrams of a 4 × 4 microchip-based stimulator and (b) the output waveforms from the stimulator in saline solution (47). The four-digit numbers are the microchip IDs.

Introducing the serial bus architecture enables the stimulator to vary in pulse parameters such as amplitude and duration for each microchip through the serial interface.

It should be noted that the number of microchips to be controlled is restricted by the asynchronous counter design and that the number could easily be increased if we design the counter with longer bits. Figure 11 illustrates the extendibility of the fabricated device: two stimulators consisting of 4 × 4 microchips with nine electrodes on each microchip (total 144 electrodes) are connected: thus, a stimulator with 288 electrodes is realized.

The Microchip-Based Neural Interface Device with Serial Bus Architecture

The broadcast architecture described in the previous section is simple but cannot realize independent control of the stimulus parameters for each microchip. In this section, we describe the next-generation microchip-based device, which integrates a single-wire serial interface, a PFM-based photosensor, an image processing circuit, and a current driver circuit [43]. Introducing the serial bus architecture enables the stimulator to vary in pulse parameters such as amplitude and duration for each microchip through the serial interface. The microchip is fabricated by 0.6-μm CMOS technology and is 500 μm × 500 μm. A microphotograph of one of the microchips is shown in Figure 12(a).

Special care is taken in the design in consideration of power consumption because we assume stimulator operation of a number of the microchips via wireless communication, which

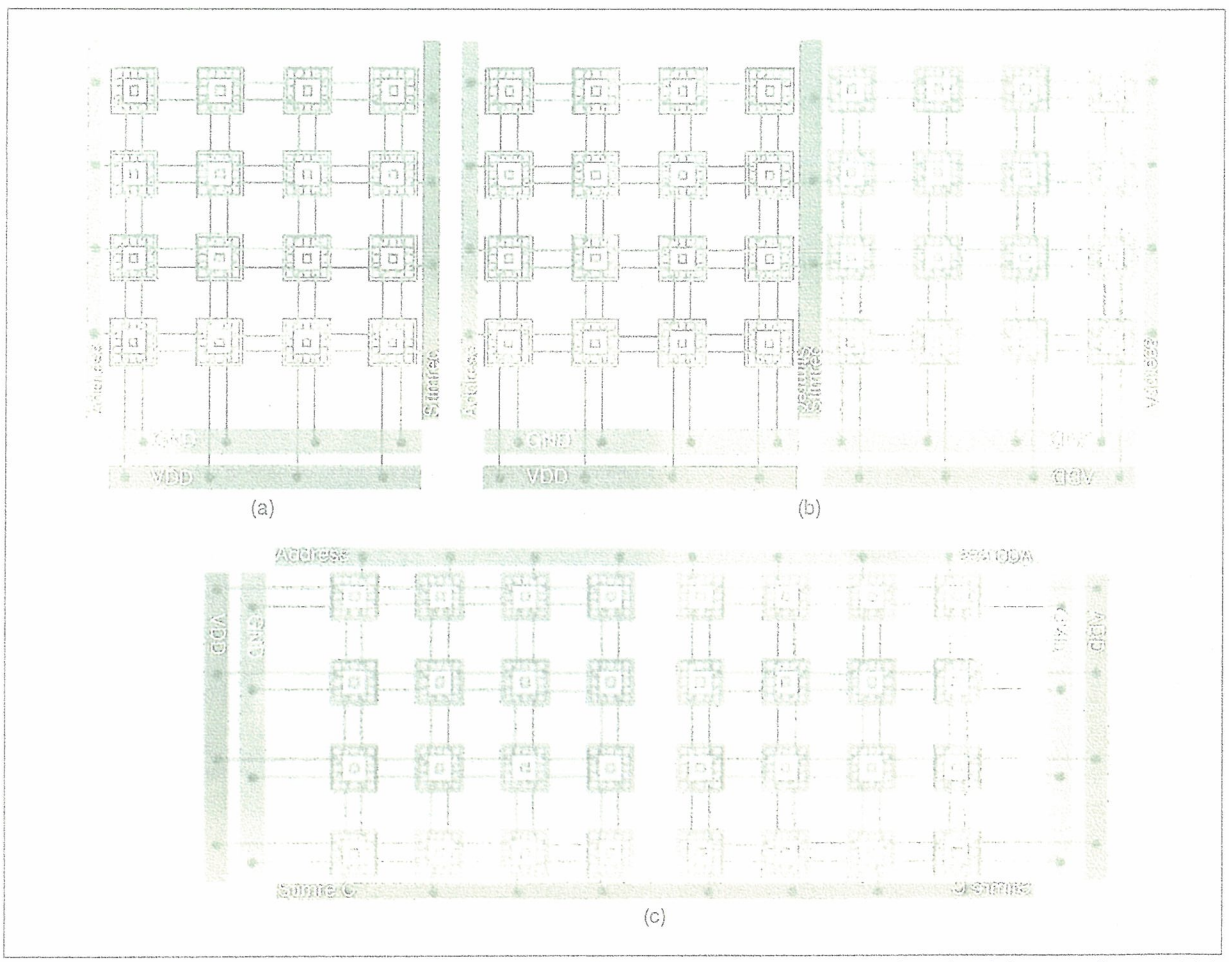

Fig. 11. Extendibility of the proposed stimulator: (a) original stimulator, (b) two stimulators with horizontal connection, and (c) two stimulators with vertical connection.